Magma chamber formation by dike accretion and crustal melting: 2D thermal model with emphasis on zircon record *

O. E. Melnik[1,2*], I. S. Utkin[1], and I. N. Bindeman[3]

[1]Institute of Mechanics, Moscow State University, Moscow, Russia

[2]Fersman Mineralogical Museum, Russian Academy of Sciences, Moscow, Russia

[3]Department of Earth Sciences, University of Oregon, USA

*Corresponding author: Oleg Melnik (melnik@imec.msu.ru)

Paper is dedicated to late Alexander R. McBirney (1924-2019), renown volcanologist and a founder of the Volcanology Program in the University of Oregon

Key Points:

- A 2D model of magma chamber growth by dike injections shows that a vertically extended system of magma batches can be formed in a few ka
- Behavior of zircon crystals is linked to thermal evolution of magma-host rock system by diffusion growth model in > 100,000 points.
- Isotopically diverse magma batches are generated naturally in an interconnected network of eruptible magma bodies with >50% melt

Abstract

Rapid progress in investigation of zircon records for U-Th-Pb ages and O and Hf isotopes in igneous rocks require understanding how magma bodies are formed and evolve in the crust. We here present a 2D model of magma bodies formation in granitic crust by injection of rhyolitic or andesitic dikes and sills. We combine this model with our zircon crystallization/dissolution software and compute zircon survival histories in individual batches of magma and country rocks.

Simulations reproduces incremental accumulation of intruded magma into magma chambers generating eruptible and interconnected magma batches with melt fraction >50 vol% that form in clusters. The rate of melt production is highly variable in space and time. The volume of eruptible melt strongly depends on the input rates of magma Q and the width W of the dike injection region. For example, dikes injection with Q=0.25 m^3/s with W=500 m during 4 ka generate 20 km^3 of melt while no significant melt forms if W=4 km. Injection of andesitic dikes produces only slightly more melt than rhyolite to granite injection despite of much larger thermal input.

Due to rock melting most of zircons loose significant portion of their old cores and, thus, average age. Magmatic zircons in the periphery of the intrusion form very quickly while in its central part crystals contain old cores and young rims and can grow during several hundreds of ka. We observe diverse proportions of crustal melt/newly intruded magma, which translates into diverse O and Hf isotope distribution in zircons.

Plain Language Summary

Magma bodies formation in the crust via its melting is important for understanding how the continental crust is created and melted and for volcanic hazard assessment. In particular, it is important to understand how much magma can be produced and stored in the crust and what is the architecture of such magma systems. As numerical methods that investigate these phenomena

50 are developing on all scales, rapidly improving dating methods of mineral zircon and its isotopic
51 and chemical content serve the purpose to recognize magma processes and their timing in real
52 geologic systems. In this paper we present a new model of magma chamber formation based on
53 intrusion of dikes and sills and offer the 2D software to do that for user-specific situations. We
54 further combine this software that produces temperature-time histories in more than 100
55 thousand points with zircon crystallization software previously published by us. We are now able
56 to describe in detail magma chamber growth and formation, and the history of zircon dissolution
57 and growth.

58

59 **1 Introduction**

60 Magma bodies formation in the crust via its melting is important for understanding how the
61 continental crust is created and melted and for volcanic hazard assessment. In particular, it is
62 important to understand how much magma can be produced and stored in the crust under active
63 volcanoes and caldera systems, what is its state, and what is the architecture of such magma
64 systems. The main mechanism of magma transport in the Earth's crust is via formation of cracks
65 along which magma rises to the surface in the form of dikes and sills (Rubin, 1995). Basaltic
66 magmas typically rise from mantle depths of several tens of kilometers carrying heat that enables
67 a multitude of melting phenomena in the crust (Huppert and Sparks, 1988; Annen and Sparks,
68 2002; Annen, 2009; Dufek and Bergantz, 2005). A common place of their ponding revealed by
69 geological and isotopic arguments (DePaolo et al, 2019), and thermomechanical modeling is in
70 the lower crust or Moho (Colon et al. 2018) for a variety of tectonic environment ranging from
71 plume to subduction zones. Their differentiation products that include basaltic andesites and
72 andesites rise from these magmatic "hot zones" (e.g. Annen, 2009) in the lower crust and intrude
73 the middle and upper crust in continental arc systems, or areas in intracontinental magmatism.
74 Dike widths can vary from centimeters to tens of meters, and in horizontal extent - from meters
75 to up to several hundred kilometers (Krumbholz et al., 2014). Magma may flow in the dikes with
76 rates of meters per second and erupt many cubic kilometers of basalts in less than a year as is
77 evidenced by historically observed eruptions such as Laki (15 km^3, Thordarsson and Self, 2003)
78 and Bardarbunga (Gudmundsson et al. 2014). Estimated magma flux rates range from 0.0001

79 km^3 in monogenetic magma fields in subduction-related environments to 0.1-1 km^3/yr in hot-
80 spot volcanoes such as Hawaii (Robinson & Eakins, 2006), or during outbursts of magmatism
81 such as those happening in Large Igneous Provinces (Costa et al. 2008; Bryan and Ernst, 2007).

82 In nature, high rates of magma injection generate significant overpressure in the upper crustal
83 magma bodies, leading to volcanic eruptions (Caricchi et al., 2014). This gives a relatively
84 narrow window of the influx rates and supply durations that can generate large eruptible volume
85 of magma suitable for super eruptions. The volcanic/plutonic ratio is an important and poorly
86 constrained parameters in many magmatic systems; higher magma rates are thought to result in
87 greater proportion of erupted materials, while low magma flux rate results in formation of
88 plutons without a connection to the surface (e.g. Glazner et al. 2004).

89 Whether mantle-derived magma will erupt on the surface without much interaction with the
90 crust, or stall in the crust, differentiate and cause crustal melting is a century-old debate of
91 petrologists, geophysicists and modelers (Becerril et al. 2013; Edmonds et al., 2019 and
92 references therein). In particular, magma ascent in dikes is controlled by the buoyancy forces
93 and the tectonic stress field among the main factors (Simakin and Talbott, 2001; Townsend et al.
94 2017). Most dikes do not reach the surface but are blocked at the level of neutral buoyancy
95 (Walker, 1989), or with structural barriers in the form of stronger rock layers or melt zones
96 (Edmonds et al. 2019). Repeated introduction of dikes into the near-surface (first kilometers)
97 region of the Earth's crust leads to mechanical dike stalling and their solidification, or upon
98 repeated flow, formation of magma chambers with or without associated crustal melting
99 (McBirney, 2006). As is evidenced from Large Igneous Provinces or supervolcanic eruptions,
100 volumes of liquid magma can reach thousands of cubic kilometers, although usually the volumes
101 are much smaller (kilometers-tens of kilometers) and globally magmatic volumes vs frequency
102 follow typical log-linear relationships (Papale, 2018). Magma chambers can be detected with
103 some success by seismic tomography using shear wave attenuation (e.g. Heath et al., 2018).
104 They may have an irregular shape, but most often appear to be flattened bodies with vertical or
105 horizontal strike. The current paradigm is that there can be several chambers located at different
106 depths under active volcanoes or caldera systems (Elsworth et al., 2014; Cashman et al., 2017),
107 not very far from a textbook example of lower (hot zone) and upper crustal magma bodies in the
108 crust (McBirney, 2006).

The numerical modeling of formation of magma chambers by injection of magma in the crust started with a pioneering work of Huppert and Sparks (1988) who used 1D heat transfer model with a realistic phase diagrams. Further development of these models into pseudo-2D and axisymmetric cylindrical coordinates (Annen et al. 2006, Annen, 2009, Dufek and Bergantz, 2005). Current modeling efforts proceed on all scales. For example, using a large scale thermechanical program of Gerya and Yuen (2003) that takes into consideration fully mechanically coupled crustal rheology, Colón et al. (2018, 2019) simulated crust-wide multi-level magma system formation under the hot-spot environment of Yellowstone on million-year timescales. In more detailed local models where penetration and heat transfer between individual dikes and sills and host rocks are considered (Annen, 2009, Dufek & Bergantz, 2005) modeling of individual magmatic outputs are possible. Models of the first type consider regions with a characteristic size of tens of kilometers and a grid spacing of several hundred meters. They cannot resolve the sub-grid heat exchange processes that occur during the real transport of individual portions of magma, but they allow to estimate the size and position of magma chambers based on the crust-upper mantle-wide distribution of temperatures, rheological properties of rocks and stresses, as well as the distribution of magma between individual chambers. In the models of the second type, the region into which magma is introduced is set in advance based on the known geological structure of the crustal block, and available geochronological estimates of the time of formation of magmatic bodies. An example of the reconstruction of a real magmatic system of Jurassic Yerington batholith in Nevada, is presented in (Schöpa et al., 2017). The model assumes horizontal sill emplacement with sinking of the underlying rock layers to accommodate the added mass, as in Annen et al., (2006). The heat equation is solved taking into account the latent heat of melting for the rocks and the real temperature dependence of the concentration of crystals in rocks and magma. An explicit scheme for solving the heat equation is used, which imposes a significant limitation on the time step and the total computational time. Biggs and Annen (2019) considered merging of two magmatic centers located at the same depth and corresponding ground deformation. They found that closely spaced intrusions can develop combined viscoelastic shells over time scales of 10s ka and form laterally extensive mush zones over time scales of 10–100 ka for the high melt supply rates and deep chambers where thermal conditions are suitable. Melt separation and migration is not considered in the model but should play significant role for lower magma fluxes.

In the model (Dufek & Bergantz, 2005), the introduction of dikes can appear in random directions within a certain crust volume. To determine the field of displacements, the rocks are considered as a viscous fluid and the Naiver-Stokes equations are solved. However, this approach does not apply for low temperatures, at which the behavior of the rocks is elastic. In (Karakas et al., 2017), the introduction of dikes is considered vertical. Each dike ends up with a sill at the top. Dike emplacements are stochastic in position and length. Rock movement is determined solely by kinematic relationships. Initially dikes are placed in the lower crust and lead to thermal maturation of the whole crustal body. Later the upper crustal reservoir is formed by dike injection into the upper crust. Simulations reveal that igneous provinces of less than a few hundred thousand years old are unlikely to support large upper crustal reservoirs, whereas longer-lived systems (active for longer than 1 million years) can accumulate magma and build reservoirs capable of producing super-eruptions.

In all these models the efficiency of crustal melting defined as the volume of crustal melt produced by volume of deep magma injected is strongly dependent on the ambient temperature, (depth of the process), and the geothermal gradient (e.g., Colón et al. 2019). Melting starts after a period of heat incubation which is dependent on the flux rate. Furthermore, the efficiency of melting varies for different sill emplacement modes: underplating (when each subsequent sill is intruded under the previous), overplating, intraplating, and random intrusion into the sill-affected areas. Expectedly, efficiency of crustal melting and crustal melt productivity is decreasing in the listed order, because overplating delivers heat directly to the melting boundary and maintains the steep temperature gradient.

In the parallel effort by geologists, the lifetimes of individual magmatic systems, large and small, arc- or hotspot related, can be understood by the ever-improving U-Th-Pb geochronological methods involving single crystal zircon studies and most recently CA-IDTIMS methods (e.g., Schaltegger et al. 2019). When considering recent (<1-2 Ma) magmatic system, resolution of individual magmatic episodes is possible on century timescales by considering zircon age spectra (Crowley et al. 2007). These recent studies demonstrated for example that silicic supereruptions with volume exceeding 1000 km^3 of eruptible magma can be generated in less than 5,000-10,000 years (which we call “Yellowstone” type), to longer than 500,000 years (which we call “Fish Canyon” type) based on concurrent CAIDTIMS efforts (Wotzlaw et al 2013, 2014, 2015). The

eruptible magma in the first case is near- liquidus, crystal poor rhyolites, while in the second case erupted magma is represented by well-mixed near-solidus mushes with 45% crystals (Bachmann et al. 2002). It is important to state that "cold and wet" arc magmatic system, the most abundant silicic magmatic factory on earth, exhibit a full transition of these behaviors, between these end-members. Glazner et al. (2004) argued that given 10 Myr spread in ages of zircons in granites of the Tuolumne Intrusive Suite of Yosemite National Park, a major batholith in the Sierra Nevada Mountains (California) are formed by accumulation of silicic magmatic dikes and intrusions over similarly long and less robust magmatic episodes (also cf. Miller et al. 2011). These may never have an active volcanic connection to the surface, and late-plutonic processes after such dike accretion, have fused them together and created relatively homogenous batholiths (Bartley et al. 2020). In other cases, there is undeniable evidence of the existence of near-all liquid magma bodies that exist in the crust in >1000 km^3 volume and erupt to the surface in the form of a single supereruption (Cashman et al. 2017; Wotzlaw et al. 2014). It can be generalized without a doubt that magmatic arcs, continental and oceanic, demonstrate a great variety of sizes and styles of the magmatic systems (Costa, 2008, Annen, 2009). We thus explore these possibilities in our 2D modeling by varying intruded magma composition (andesite or rhyolite), flux per km^2, and demonstrate below that flux and distribution of flux are the two parameters that can explain multitudes of these observations.

Zircon is extremely resilient igneous mineral that can record multiple magmatic episodes. Its crystallization is related to saturation and crystallization in T-X(compositional) space (Watson and Harrison, 1983; Bindeman and Melnik, 2016). When combined with a phase diagram of a magma, zircons can help understand temperature history of magmas and rocks that undergo melting-crystallization phenomena (e.g., Claiborne et al. 2010b 2018; Melnik and Bindeman, 2018). Zircon also record isotopic values of its host magma batch, and, in particular, crustal and mantle magma proportions via O and Hf isotopes, and % remelted hydrothermally altered rocks (low-$d^{18}O$ zircons). Studies of example of recent magmatism demonstrate that zircons commonly show extreme O and Hf isotope diversity but have an unresolvable U-Pb eruption age (e.g., Wotzlaw et al. 2014; 2015). This demonstrates the need of mixing between isotopically diverse magma bodies that are simultaneously present in the crust (Bindeman and Simakin, 2014; Colon et al. 2019).

Links between zircon evolution with thermal maturation of the magma-rock system is studied by (Caricchi, Simpson, et al., 2014) and (Caricchi et al., 2016) with a 2D axi-symmetric model of magma injection. These authors considered generic magma flux and temperature evolution of the system, coupled with randomized sampling of eruptible magma regions (where proportion of melt exceeds 0.5) to explain formation and eruption of large volume silicic ignimbrites. A simple criterion is used for zircon age distribution based on the difference between time when magma becomes zircon saturated and cools below the solidus. Kinetic effects of zircon growth are not considered.

In this paper we are motivated to further interrogate questions of crustal melting without prescribing a geometry and displacements to the intrusions, in this sense we get a detailed view of melting and magma accumulation processes across the growing magma body. We further investigate how does the rate, distribution, and composition of magma flux into the crust influence the distribution of zircon populations.

Therefore, this paper pursues two main goals. We first present a new generic 2D model for heat and mass transfer during periodic injection of andesitic and rhyolitic dikes and sills into the granitic host rocks that allows variable direction of dike emplacement, dike to sill transition, country rock melting, and elastic rock displacement. Such 2D model, and software, have not yet been presented to our knowledge. The model uses simplified T-X phase diagram representing melt fraction, X as a function of temperature, T. Second goal is the integration of this model with zircon growth-dissolution software of (Bindeman & Melnik, 2016) that reads temperature-time-melt fraction properties in a Lagrangian particle. Thermal histories recorded by rock and individual magma parcels are thus used for estimation of zircon crystals evolution and their survivability and average growth ages in the entire magma body. We further monitor the fraction of eruptible magma in different parts of the model and estimate the proportion of crustal rock melt produced by newly injected magma. We next estimate O and Hf isotopic values in different parts of the intrusion at assumed and typical O and Hf isotopic end-member compositions of the crust and the mantle.

2 Materials and Methods

2.1 Mathematical model

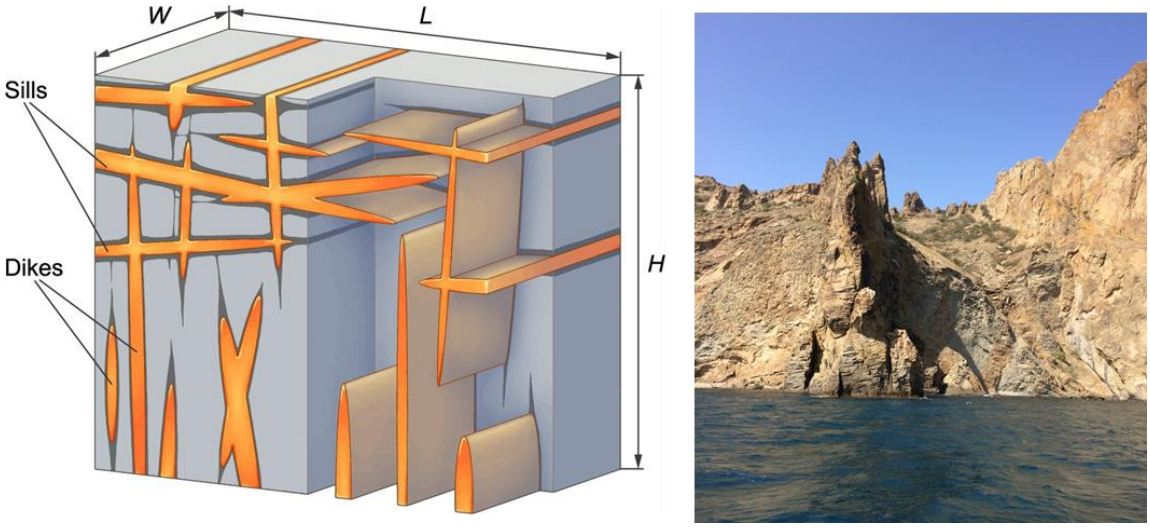

Figure 1. A) Set-up of the model showing intersected network of dikes and sills causing melting of country rocks. B) mid-Jurassic Karadag pluton (coastal Crimea) showing similar ellipsoidal dike structure, with columnar jointing marking each individual dike. (photo by A. Tugolesova)

Set-up of the model is presented in Fig. 1. We assume that injection occurs in 2D plain geometry, model individual dike as an ellipsoid with semi-axes *a* and *b* and use analytical solution (Muskhelishvili, 1977) in order to calculate host rock displacement. Each dike contains either andesitic or rhyolitic magma with a specified temperature, while host rocks are granitic in composition and are elastic with fixed properties. Initial temperature distribution is linear with a specified geothermal gradient. Injection of individual dikes leads to displacement of elastic host rocks and initiates heat transfer that causes country rock melting and intruded magma solidification. Volume of the individual dike and the frequency of emplacement is controlled by the specified influx rate of the magma Q_{in} (km^3/y). The flux is laterally varied per different simulations from defocused to more centrally focused by specification of a normal or uniform distribution of the coordinates of the dike centers. In order to calculate the volume of the individual injection, the third spatial dimension is specified at L= 2 km and kept constant. This situation is possible in the extensional tectonic environment, where the local stress field leads to preferentially parallel dike orientation. We allow random angle for the individual dike

emplacement or the change in the dike orientation from sub-vertical at depth to sub-horizontal near the surface reflecting dike to sill transition (Barnett & Gudmundsson, 2014).

$$
\begin{aligned}
&\rho C\left(\frac{\partial T}{\partial t}+\vec{V}grad\left(T\right)\right)=div\left(k\,grad\left(T\right)\right)+\rho L\frac{d\beta}{dt}\\
&\frac{\partial \alpha}{\partial t}+\vec{V}grad\left(\alpha\right)=0\\
&\rho C=\rho_r C_r\left(1-\alpha\right)+\rho_m C_m\alpha\\
&k=k_r\left(1-\alpha\right)+k_m\alpha\\
&\beta_r=\beta_r\left(T\right),\beta_m=\beta_m\left(T\right).
\end{aligned}
\tag{1}
$$

Rock and magma temperature evolution *T* is governed by heat conduction equation (1) that accounts for advection due to rock and magma displacement, latent heat of crystallization and heat conduction. Here ρ is the density (indexes "r" and "m" reflect rock and magma respectfully), *C* is the heat capacity, $\vec{V}$ is the advective velocity, *k* is the conductivity, *L* is the latent heat of crystallization, β is the mass fraction of crystals that depends on temperature according and magma type (see Supplementary Fig. S1 for $T-\beta$ diagrams), α is the volume fraction of magma in the rock-magma system.

The emplacement of a dike is considered instantaneous, therefore, the velocity field $\vec{V}$ is determined based on the displacement field $\vec{U}$ arising from the loading of an elliptical crack. The values of the semi-axes *a* and b, as well as the angle of dike injection are set randomly at certain intervals. The number of dikes that are emplaced during a time step is calculated in such a way that the average increase in magma volume is equal to a given magma influx rate for the area. Rock displacements depends on dike overpressure, that can be determined from the width of the dike *b* at a given length *a*, based on the solution (Muskhelishvili, 1977):

$$
\Delta p=\frac{bE}{a\left(1-\nu\right)} \tag{2}
$$

Here, *E* is the Young's modulus and ν is the Poisson's ratio of the host rocks, which are assumed constant in the present study.

We postulate elastic rock response in our model to keep mechanical problem relatively simple and separated from the thermal model in this study. Account for viscoelastic properties of rocks

and solidifying magma, heterogeneities of rheological properties within the domain, volatile exsolution and transport, local tectonic stresses and other complexities will require solution of a coupled thermo-mechanical-chemical problem that is extremely difficult for wide ranges of physical properties of the system. Clearly, the model captures well the initial stage of magma chamber formation when the melt volume fraction is relatively small, but we expect deviations in velocity field calculations as the system matures.

2.2 Numerical method

Discretization of equations (1) is carried out by the control volume method with operator splitting in spatial coordinates (Patankar, 1980). For each coordinate direction, the system of linear equations resulting from discretization is solved by the tridiagonal algorithm, which makes computations stable at larger time steps unlike explicit modeling schemes previously employed.

Since the dependence of the melt fraction on temperature (T-X, diagram, Fig. S1), as well as the thermophysical parameters of the rocks can differ for magma and surrounding rocks, the volume fraction α of the introduced magma is stored in each cell of the computational grid. Injection of a new dike leads to advection of the volume fraction in accordance with the displacement field around the dike. Grid-based methods, such as method of characteristics, suffer from significant numerical diffusion, which leads to unphysical mixing between magma and surrounding rocks.

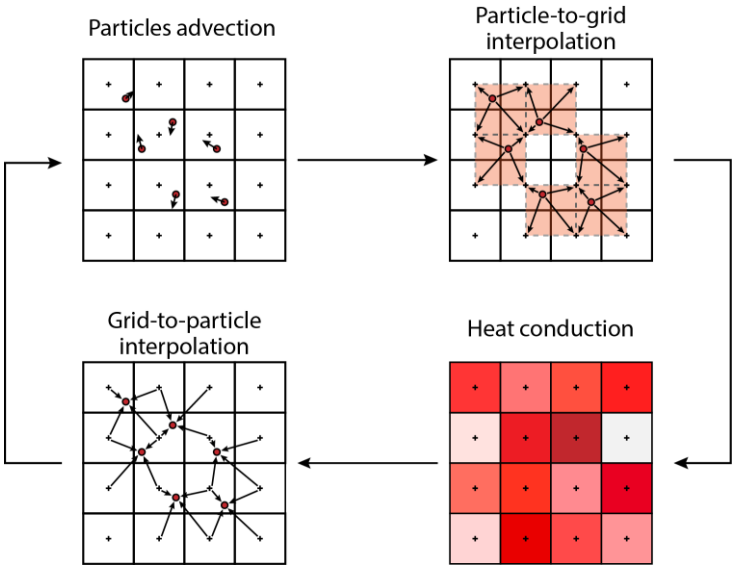

Figure 2. Outline of the PIC method used for advection of temperature and volume fraction.

To reduce numerical diffusion, the hybrid PIC / FLIP method is used to determine the volume fraction of magma and for advection of the temperature field. As shown on Fig. 2, in addition to the grid, the continuous medium is also discretized by a set of marker particles that store a flag indicating whether a particle belongs to magma or surrounding rocks, as well as the temperature at a point in space corresponding to the coordinates of the particle. Since the displacement field is determined from the analytical solution, for each particle its displacement can be calculated precisely. After that, the volume fraction of magma at grid cell centers is calculated by bilinear interpolation from each particle to the four cells closest to the particle. Thus, the numerical diffusion for the transfer of the volume fraction of magma is significantly reduced.

Since the heat conduction equation is additionally solved for the temperature field on the grid, according to the original PIC method, it is necessary to interpolate the temperature from the grid back to the particles. It can also lead to numerical diffusion of the temperature field. The FLIP modification to the PIC method, developed by Brackbrill and Ruppel (1986), is designed to interpolate not the temperature field itself, but only the difference between the temperature obtained by interpolating from the particles onto the grid and the temperature after solving the heat conduction equation. This significantly reduces numerical diffusion but leads to the unphysical noise in the regions with large temperature gradients, e.g., on the boundary between the dike and rocks. A common solution to this problem is to add a small fraction of PIC interpolation to the result, usually about 5%, which makes it possible to smooth out these oscillations by adding a small amount of scheme diffusion, which is negligible compared to physical heat diffusion due to thermal conductivity.

When a new dike is introduced, new particles are generated. If any of the grid cells contains too many particles as a result of elastic compression of the medium, excess particles are destroyed. We stop tracking a particle when it reaches the boundary of the computational domain. If there are too few particles in the cell due to the stretching of the rocks, new particles are created, and the values of temperature and volume fraction in them are interpolated from the grid.

We use fixed grid spacing of 5 m for temperature calculations. This results in 2000x2500 grid points in the computational domain. The code was tested on analytical solutions of 2D heat exchange problems.

3. Results

The model presented above allows users to study a wide range of magmatic phenomena. The code is written in Julia programming language (julialang.org) and individual simulation setup is governed by a run file that utilizes YAML markup language capabilities to specify physical properties of the rock and magma, depth, distribution, angles and sizes of injected dikes, proportion of dikes to sill and dike to sill transition and distribution vs depth, magma emplacement schedule with different influx rates and durations for each injection episodes. Results of the simulations are stored in hdf5 files for mesh related variables and .csv files for individual Lagrangian particles that are used as input conditions for zircon growth/dissolution simulations. The program and algorithm are accessible to anyone with minimal programming skills and is designed to be modified by the users to their specific situations, for example for studies of individual magmatic and caldera systems.

Below we present examples of application of our approach to typical island arc situations. The results of this modeling show capabilities of the model and mimic basic scenario for the formation of magma chamber by rhyolitic and andesitic magma intrusions.

3.0.

3.1. Rhyolitic and andesitic dike injection into granitic crust

We first present simulation results for magma (0% crystals, T=900 °C) of rhyolitic composition injected sequentially as dikes and sills into the crust of the same, fully crystalline granitic composition. Depths of injections varies between 5 and 12 km, with an initial temperature gradient of 20°C per km, with a given temperature at the top of 200 °C and 500 °C at the bottom of the injection zone, typical depths of crustal magma chambers and batholiths. This setup simulates formation of upper crustal plutons and magma bodies containing eruptible magmas. Parameters that are used in simulations are listed in Table 1.

Parameter	**Description**	**Value**
ρ	Density	2650 kg/m^3
λ_r	Thermal conductivity of rock	1.5 W/m/K
λ_m	Thermal conductivity of magma	1.2 W/m/K
C_p	Specific heat capacity	1350 J/K/kg
L	Latent heat of melting	3.5×10^5 J/K/kg
T_m	Magma intrusion temperature	Andesite: 1100 C Rhyolite: 900 °C
T_{top}	Temperature at depth z = 5km	200 °C
ΔT	Temperature geothermal gradient	20 °C/km
ν	Possion's ratio of rock	0.3
E	Young's modulus of rock	15.6 GPa
Q_{in}	Intrusion rate	0.25 – 1 m^3/s
$[z_{min},z_{max}]$	Dike center depth	6 – 14 km
w	Half-width of dike intrusion region	250 – 2000 m
$[zs_{min}, zs_{max}]$	Depth range of sills formation	6 – 8 km
θ	Dike rotation angle	85° – 95°
a	Dike length	200 – 3000 m
b	Dike thickness	10 – 20 m
h	Dike transverse width	2000 m

Table 1. Parameters used in the simulations

Fig. 3 presents the graphical results of calculations of the melt fraction and temperature evolution during formation of a magma chamber at different stages of its growth and cooling. Magma injection rates are taken as Q = 0.5 and 1 m^3/s (0.015-0.03 km^3/year), and few simulations below consider lower 0.25 m^3/s rates. Dikes are introduced sub-vertically in the range of depths from 12 to 5 km. The injection zone grows in vertical and horizontal as the system swells by vertical and lateral extension (Fig. 3). Given that dike intrusions are changing orientation to sills as is abundantly seen in nature (Fig. 1b, McBirney, 2006; Thomson, 2007) and experiments (Menand et al. 2010), we adopt such transition in the model. We assume that if the center of the dike is at a

depth between 6 to 8 km, then the emplacement of the magma becomes sub-horizontal (sills). Such situation is common in the areas of active volcanism and may be associated with the distribution of the density of the host rocks (level of neutral buoyancy for the magma, (Walker, 1989) or the presence of layers with a larger Young's modulus (Barnett & Gudmundsson, 2014). The analytical solution that is used to calculate the displacements of host rocks in current model cannot be applied for the latter case as it assumes homogeneous elastic rock properties.

In current set of simulations injection takes place during first 4000 years (4ka), followed by a subsequent cooling for 750,000 yr (750 ka). No volcanic eruption (removal of melt and heat) is allowed; however, we track percent and distribution of areas with >50% (eruptible magma), and >1% melt (solidus), and % of crustal melt vs intruded melt throughout the intrusion. For low injection rate ($Q = 0.5$ m^3/s) emplacement of dikes into W=4 km width region of the crust forms patchy distribution of molten rocks with observed low connectivity in between during the intrusion period (Fig. 3). Due to heat transfer after the injection and melting of country rocks the connectivity and sizes of individual batches of magma progressively increase while their melt fractions decrease. After ~300 ka temperature drops below the solidus at every point and the magmatic system solidifies completely into a mid-crustal pluton consisting of a series of closely spaced and accreted dikes.

Larger influx rate ($Q = 1$ m^3/s) leads to a formation of fully molten magma body, maintaining the 100 % melt fraction in its center even after 100 ka of cooling if magma injected in a narrower region (W=2 km). In the case of wider distributed magma flow W=4 km, a magmatic system is formed with high melt fraction and small batches of fully molten magma. In the latter case, the overall lateral proportion of dikes is larger than the injection area due to displacement of the host rocks and previously injected magma.

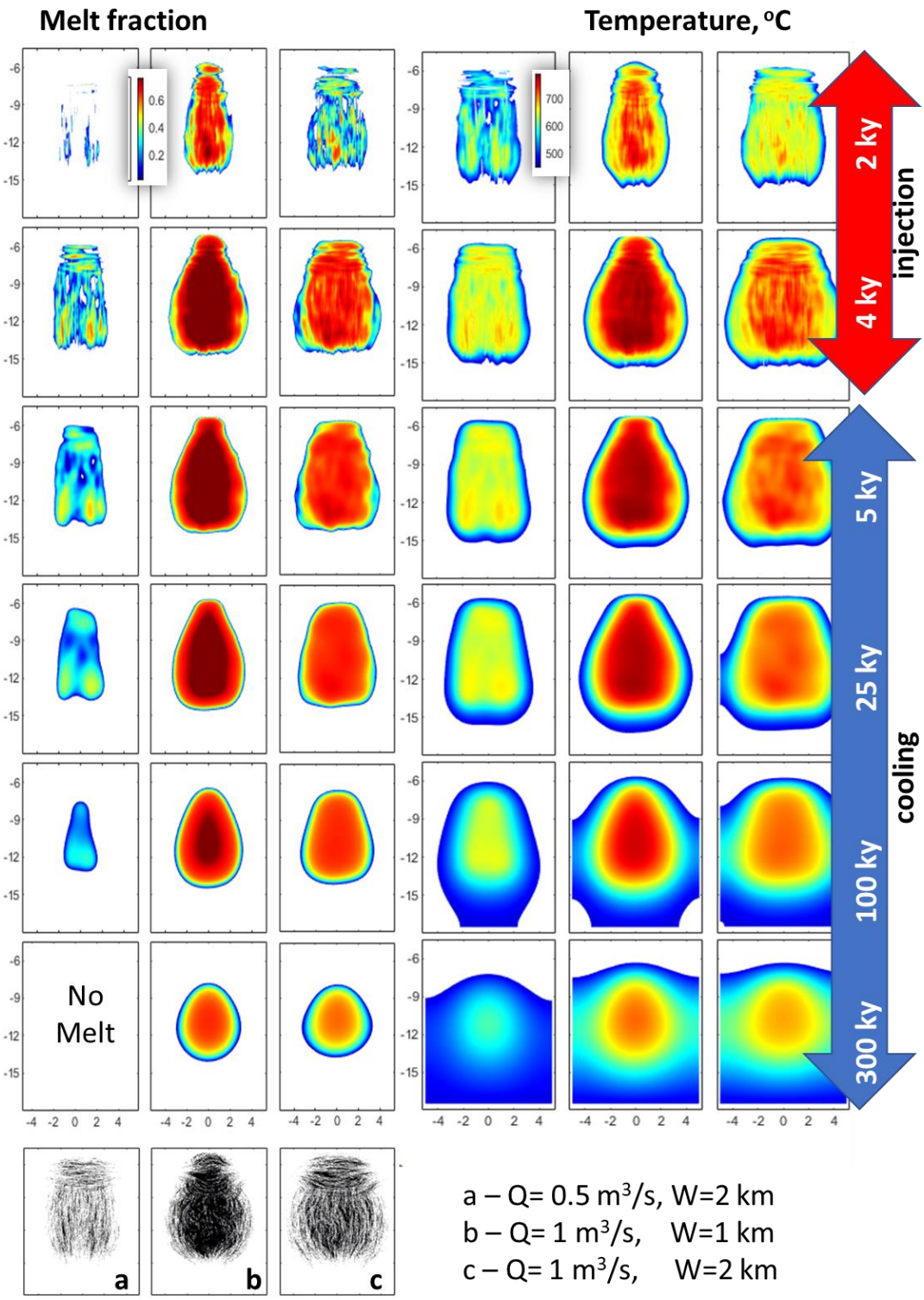

Figure 3. Evolution of melt fraction and temperature in the magma body grown due to sill and dike injection. Each vertical column represents a separate case with a different rate Q, and injection zone W. Magma injection time is 4 ka followed by magma cooling without injection.

This case only considers rhyolitic dikes intruded into a granitic crust of similar composition. For andesitic magma intruded into the granitic crust, see Fig. S2 in the supplementary material.

Fig. 4 shows kinematics of Lagrangian particles associated with rocks and magma. In the dike injection region displacement is preferentially horizontal and downward, while intrusion of the sills leads to a vertical displacement (uplift) of several hundred meters. Particles near the central line of the intrusion exhibit small horizontal shift, dikes injected at later stages stay within the injection region, while the early injected material is pushed to the periphery of the intrusion, in a fashion similar to spreading. The total displacement during active diking period lasting 4 ka exceeds 2 km at depth and a few hundred meters near the surface, while thermal equilibration length-scale on this timescale is of order of 300 m. It means that during the formation of the magma chamber heat transfer and balance is dominated by advection and latent heat release/consumption. This is a novel result of our 2D simulation with elastic displacement, not seen in previous 1D models.

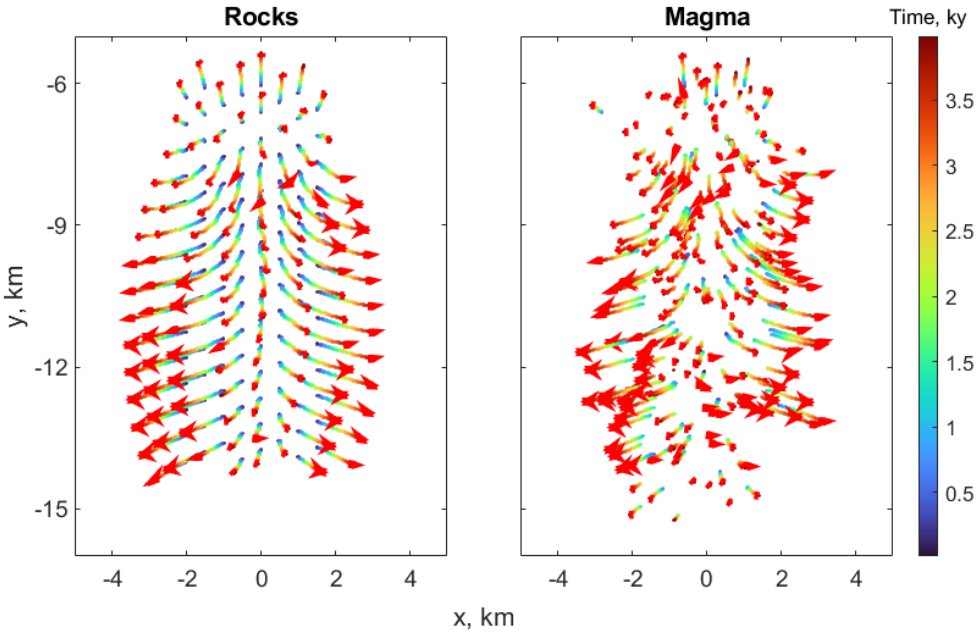

Figure 4. Displacement of Lagrangian particles associated with magma (right) and rocks (left). The time of dike emplacement is shown by color. Note the "Christmas Tree" sagging pattern in the lower part of the model and an uplift in the upper part.

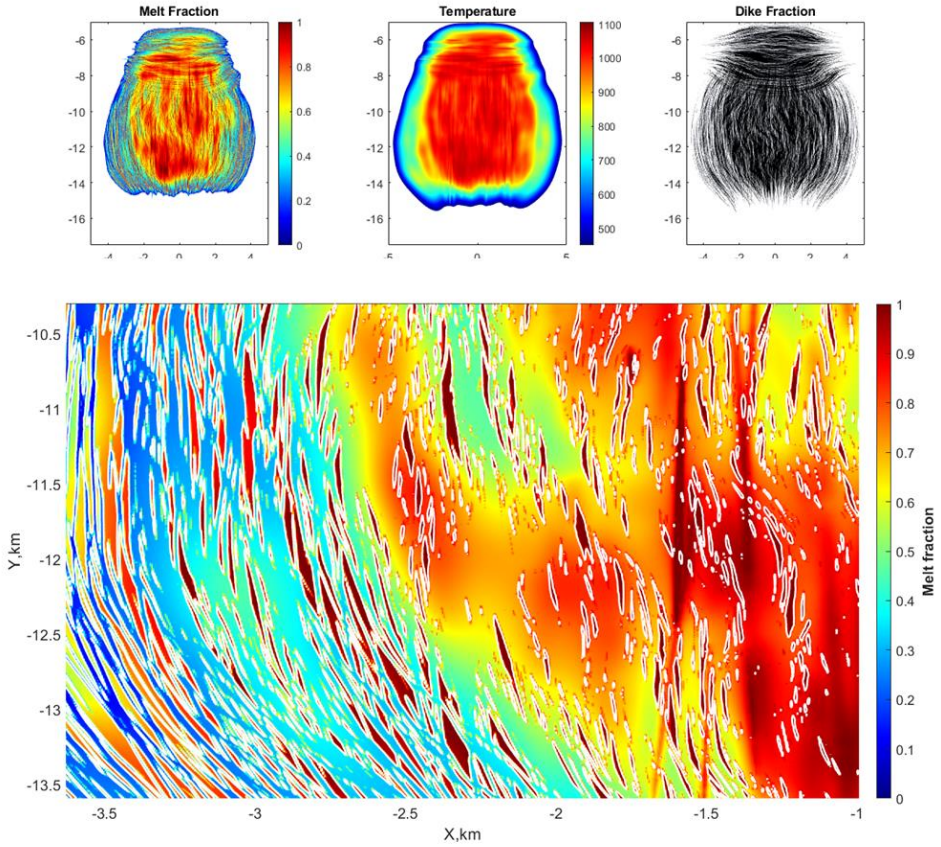

Figure 5. Distributions of the melt fraction, the temperature, and dikes in the case of injection of the hotter andesitic magma into granitic crustal rocks with Q = 1 m^3/s. Note high melt fractions and connectivity in the right-hand side of the model. The shown region can be treated as largely molten interior and partially molten contacts.

We next consider a case when hotter andesitic magmas are intruded into the granitic crust (Fig. S2). Like is the case with the rhyolitic dike injection, first andesitic dikes freeze without melting, and an incubation period of several hundred years is required before the system is able to sustain sizable and growing magma volumes. The behavior of andesitic -granite system is also different because of different composition of the intruded dikes and greater liquidus-solidus separation, which affects composition of the partial melt that is stored in andesitic dikes at different time and place. However, and perhaps counterintuitively, hotter andesitic dikes do not produce more melt in the system. Fig. 5 shows distributions of the melt fraction, the temperature, and dikes in the case of injection of the hotter andesitic magma into granitic crustal rocks with a high flux rate Q = 1 m^3/s after 4 ky of magma influx. Distribution of the melt fraction is patchier than in the case

of injection of rhyolitic magma. Zoom out of the lower portion of the intrusion is shown on the bottom panel where fully molten regions are associated with the remaining host rocks and newly injected dikes, meanwhile magma injected earlier shows variable degree of remaining partial melt. Intrusion of andesitic dikes generates rhyolitic partial melt in the country rocks and a residual melt of variable SiO_2 as interstitial in andesites. At large melt fraction, melts would segregate and higher temperature restites would sink, but this is not modeled in this work.

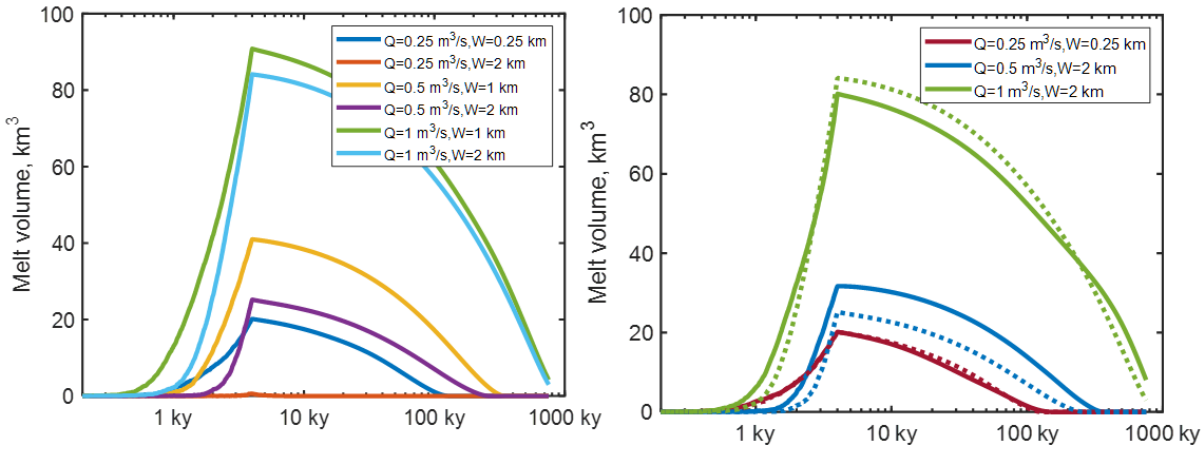

Figure 6. Melt volume fraction for different injection rates and width of the domain (a) – rhyolite to granite. (b) – andesite to granite. Intrusions continue to 4 ka after which they stop and the system cools. Note the incubation period needed for preheating of the crust on the order of 500 yrs, followed by a rapid onset of melting. Andesites intruding granite generates the same amount of total melt because at lower temperatures andesitic crystallize more (see phase diagrams on Fig. S1).

3.2. Variation in the Magma influx rate

Efficiency of melt production and formation of molten magma bodies strongly depends on the magma influx rate into the upper crust. Fig. 6.a presents the dependence of melt volume in time for four-fold change in the magma influx rates Q from 0.25 to 1 m^3/s. At these flux rates, over 4 ka the total injected magma volume varies from 31.5 to 126.3 km^3, respectively. The effect of this magma flux is however strongly dependent on the total widths of the injection region (magma focusing). Variations in the flux rate and the width results in dramatically

different outcomes for magma productivity and the efficiency of crustal melting (Fig. 6). Low influx rate injection of rhyolitic magma (Q = 0.25 m^3/s) over a wide region W=4 km, produced only 0.2 km^3 of melt at 4000 years, and nearly 20 km^3 if dikes are focused and W= 0.5 km. At higher influx rate there is still a significant influence of the dike focusing on the produced total melt volume. At high overall magma intrusion rates of Q = 1 m^3/s the dike focusing influence is rather small.

Change in the magma type from rhyolite to andesite again surprisingly results in a comparable overall melt production, due to rapidly changing melt% with a decreasing temperature in the andesitic phase diagram (Fig. S1). Although the temperature of andesitic magma (solid lines on Fig. 6.b) is 200 ^oC higher than for the rhyolitic magma (dashed lines), melt volumes produced by both magmas are similar and are controlled by the injection rate and the region width. Melt production for the case of andesitic magma intrusion starts slightly earlier than for rhyolitic due to more rapid melting of the host rocks by hotter magma.

3.3. Percent country rocks vs magma differentiate and its variation with time

Fig.7 represents exploration of the extents of crustal melting by rhyolitic magma intrusion by specifically tracking the regions with country rock melting (>1%), and for eruptible magma (in which total melt fraction exceeds 50%). This number is taken as a simple measure or rheological extractability of magma from mushy zones (e.g. Marsh, 1981; Huber and Parmigiani, 2018). We explore different magma flux rates identical to Fig. 6, resulting in dramatically different total magma production. The ratio of country rock melt to intruded magma melt in the eruptible magma (Fig 7a) has slightly different patterns. First, proportion of crustal melt is increasing with time but reaches its peak before the end of magma injection period at 4 ka, as the injected magma dilutes the melt zones with newly intruded magma. This is a combination of cooling and melting as well as spreading of the melt zones. Regardless of the robustness of magma production (greater flux Q at narrower zone W) amount of crustal melt and the pattern of its increase remain approximately the same with slightly different rise time. Less robust magmatic systems (e.g. Q=0.5 m^3/s, W=4 km) exhibit expectedly slower increase in total melt (Fig. 6) and crustal melt production (Fig. 7a). Upon cessation of intrusions, for most cases except one for least robust magma system (Q=0.5 m^3/s, W=4 km), percent of crustal melt relative to intruded magma in dikes drops quickly, likely because the crustal melt in our model is located on

contacts of intruded dikes and thus cools quicker by conduction. In real magmatic system where melts are given a chance to segregate, this may not be the case. Nonetheless, the total amount of eruptible crustal melt never exceeds 15-20%, suggesting that in all cases it is cooling and crystallization of intruded magma that dominates the system. Additionally, because our model allows for the spreading of particles upon magma injection, country rocks are advected away from the heat source faster than the thermal diffusion is capable of melt them. This leads to lesser efficiency of crustal melting than it is possible to achieve in psudo-1D models. For example, overplating in such models always keeps the upper melting boundary hot (Annen et al. 2006) leading to significant up to 50% efficiency of crustal melting.

The melting efficiency defined as a total melt volume divided by the volume of injected magma (Fig. 7b) shows patterns comparable to total melt production (Fig. 6). Expectedly, least robust magma system (Q=0.5 m^3/s, W=4 km) have least efficiency peaking at 15%. Most other flux (Q) and width (W) combinations operate with 60 to 70% efficiency, with melt dominated by the intruded hot magma. Melting efficiency drops with cessation of new magma intrusion as the whole system crystallizes reducing melt volume (Fig. 3).

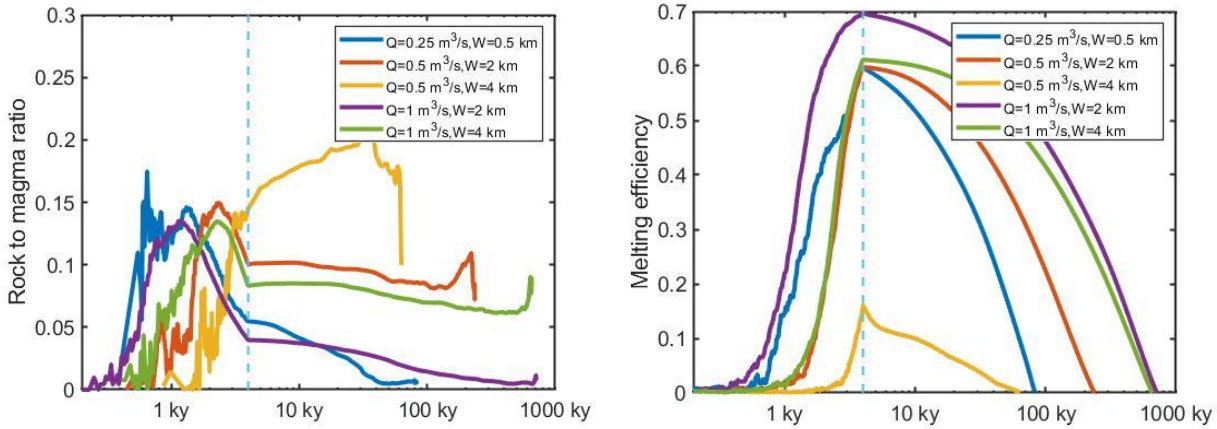

Figure 7. Crustal melting and its efficiency in the model runs with indicated magma flux Q and width of intruded area W. Vertical dashed line represent a point when magma intrusion stops at 4ka, and the cooling of the whole system begins. a) Rock to magma ratio in cumulative areas within the model where melt fraction is greater than 50%, meaning to represent potentially rheologically-extractable and eruptible magma. b) Temporal variation of melting efficiency

defined as total melt volume (melt fraction >1%) divided by the volume of injected magma. Efficiency peaks at the end of magma intrusion at 4 ka and the decreases as magma system cools and crystallizes.

Rock to magma ratio is drastically different in the case of andesitic magma injection in granitic crust (Fig. S3C). In the case of wide injection area or low magma flux magma solidifies very quickly and melts host rocks resulting to close to one rock to magma ratio. At higher or more confined magma flux up to 30 % magma remains molten end eruptible.

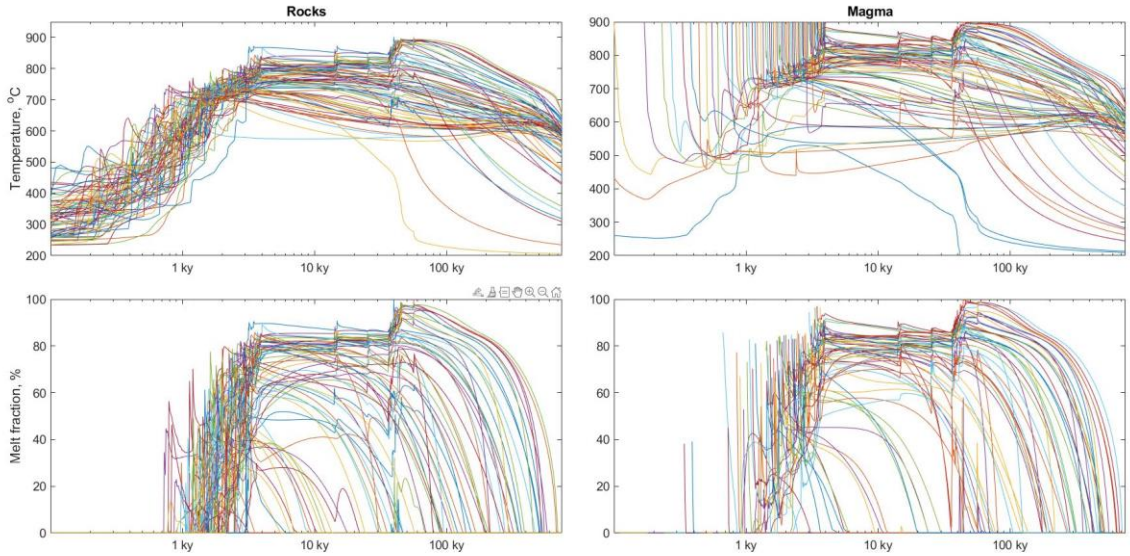

Fugure 8. Temperature and melt fraction variation in granitic rocks (a-b) and rhyolitic magma (c-d) parcels with time for Q = 0.5 m^3/s and W=0.5 km. Main dike intrusion period lasts for 4 ka, three 1000-year episodes of dike injection occur each 10 ka resulting in spikes in temperature during cooling of the magma chamber.

3.3. Magma and host rock thermal histories

The 2D model presented in this work not only allows investigation of the cumulative thermal (and compositional, % crystals) evolution of the whole system as was done in the previous models but permits investigation of the behavior experienced by multiple areas within

the growing magma body and country rocks, as well as inside of each dike or a sill (Fig. 1). Country rocks, and previously intruded and now solidified dikes can experience a non-trivial, spatially- and temporally independent series of heating, melting and crystallization episodes. Thus, the real 2D model presents a more realistic scenario for natural situations, and these changes will be reflected in their crystals including zircons. Furthermore, consideration of elastic displacement of rocks after intrusion in our model (spreading), provides an additional, previously underexplored feedback between mass and heat advection, melting and crystallization in different parts of the system.

Fig. 8 shows the dependences of the melt fraction and temperature on time for magma particles and host rocks for injection of rhyolitic dikes in granitic crust for Q = 0.5 m^3/s and W = 0.5 km. Each magma injection cools down quickly and completely solidifies during first 1-2 ky, but later intruded, and country rock melt fractions persists for a long time, until the temperature of the whole magma bodies drops down below the solidus. Occasional, late-stage intrusions (three spikes in Fig. 8) results in slight temperature and melt fraction increases. Rocks are not significantly melted by the magma at the first stage of the injection, but the degree of melting reaches more than 80% at later stages of magma chamber formation. Variation of temperature and degree of melting in an individual particle is non-monotonic and experience several heating and cooling episodes depending on its location within the area of dike injection. For example, early dikes cool down quickly and are later displaced to the periphery of the forming magma chamber. At the same time, dikes in the center remain hot and are later remelted and their melt is then reincorporated into the large body of the magma chamber. With progressive dike addition, subsequent dikes deliver heat and mass to a maturing reservoir those temperature increases smoothly. Upon cessation of new magma addition, its temperature decreases monotonically with time, while reservoir attains more spherical shape with respect to its thermal halo and melt distribution (Fig. 3). Later parcels of magma experience more complicated t-T path. The temperature and melt-fraction-time history that we observe in our 2D model both confirm “spike, then exponential decay” schemes often shown in modeling and petrologic literature dealing with magma intrusions (Caricchi et al.,2014; Szymanowski et al., 2017), used for example o model solution-reprecipitation of crystals with complex zoning. However, they are different in several important aspects. Initial stage of magma chamber growth is characterized my highly inhomogeneous temperature distribution. As magma chamber matures newly injected dikes do

not change its thermal state significantly because the volume of individual intrusion is much less than the volume of accumulated melt. Periodic unrests of the system do can locally result in large temperature increases but the average cooling trend continues.

Temperature histories for andesitic magma injection into granitic crust are presented and discussed in Supplementary material, Fig. S4. In comparison with Fig. 8 many of rock parcels become completely molten and stay molten for a long time, especially at high Q values. Hardly any magma parcels stay completely molten after injection except in the case of consolidated magma flux (Fig. S4b). This is very different from prescribed fixed position injection of the magma simulated in previous models where newly injected magma is always separated from host rocks by previous injections.

Overall temperature and melt fraction evolution in our 2D model inform us on new developments as a result of proper accounting for whole system spreading at rates faster than heat conduction. In some central parts the system exhibits behavior consistent with "overplating" models in which newly injected melt occupies the magma/rock boundary, and maintain rapid temperature rise and melting, most other parts of the model exhibit less melting that even in the random dikes and sills models of Dufek and Bergantz (2005) or Annen et al. (2006). Overall, T-Xmelt-time trajectories of the different parts of the modeled magma system experience extreme diversity, that span prescribed overplating to random dike regimes. Overall, such melting is less efficient and reflect processes in the real growing magma system.

The model further informs us on realistic Time-Xmelt-time trajectories that can be used in modeling of crystal destinies. For example, zircon (and other mineral) zoning patterns, can be now modeled and interpreted more realistically than previously prescribed spike-then decay schemes.

3.4. Zircon evolution

An important method of investigation of plutonic and volcanic system to understand their formation is evolution is provided by examining their crystal record, among which zircon petrochronology is playing increasingly more important role. Not only domains within zircons

579 can be dated with ever improving precision informing on the duration of zircon growth and
580 inheritance, but also the trace elemental zoning pattern within zircons can provide information on
581 T-X(%melt)-time changes (Claiborne et al. 2010; 2018; Melnik and Bindeman, 2018). This is in
582 addition to the use of the O and Hf isotopic values within zircons that informs on whether they
583 represent products of crustal melt, newly intruded magma, or product of remelting of
584 hydrothermally altered rocks (e.g., Bindeman and Simakin, 2014; Wotzlaw et al. 2015; Colón et
585 al. 2019).
586 This paper adds to these tasks by examining zircon behavior in the course of magma
587 body construction and cooling. For this purpose, we use temperature and compositional history
588 recorded in each marker points (50,000 total markers) related to the spatio-temporal evolution in
589 host rocks and magma and integrate these with zircon crystallization-dissolution software of
590 (Bindeman & Melnik, 2016). This relatively straightforward coupling enables reconstruction of
591 dissolution and growth histories of great multitude of individual zircons of the entire system. For
592 example, depending on the time, composition, and the position of the injected magma zircons in
593 it can 1) crystallize rapidly (years-decades) during complete solidification of magma short after
594 its emplacement or 2) crystallize over a prolonged period of time if magma is injected into the
595 hot interior and thus remains molten in a long time and cools slowly with the whole system, 3)
596 crystallize from a dike or a country rock melt inheriting their respective O and Hf isotopes, or 4)
597 first crystallize then dissolve multiple times. Zircons in the country rocks can undergo variable
598 amounts of partial dissolution depending on the temperature-time history of each particular
599 marker and preserve or not preserve the inherited core and completely or partially reset of their
600 ages and O and Hf isotopic values. Given the new 2D thermal approach presented in this paper,
601 similar modeling can be implemented for any other accessory mineral for which there is
602 diffusion and saturation conditions, or a major mineral for which the phase diagram relations can
603 be specified.
604
605 We have performed a series of such computations of zircon destinies for 50,000 of markers
606 located inside of the growing magma body. Fig. 9 shows the evolution of the melt fraction (up),
607 temperature (middle) and zircon radius (bottom panels) recorded in two magma parcels. Solid
608 line corresponds to an early injected dike, dashed – to the dike injected at the end of the
609 magmatism. In the first case magma solidifies completely and is getting remelted several times.

610 We start with zircon evolution simulation from the last complete solidification episode assuming
611 that the crystal is has initial size R_z governed by the bulk concentration of zirconium C_{bulk} in
612 magma calculated as:

613 $$R_Z = \left(\frac{C_{bulk}}{C_Z} \right)^{1/3} L_{cell};\ C_Z = 490,000\,\text{ppm} \quad (3)$$

614 Here C_z is the zirconium concentration in the zircon, L_{cell} is the size of the cell from which the
615 crystal is growing or dissolving. This parameter is specified by the number density of zircon
616 crystal N_z per unit volume $L_{cell} = \left(1/N_Z \right)^{1/3}$. Smaller number density of the crystals will result in
617 larger cell sizes, and larger initial zircon radius (see Bindeman and Melnik, 2016 for more
618 details). We assume total Zr concentration in the granitic crust is 150 ppm and in intruded
619 magma has 50-150 ppm. We use Boehnke et al. (2013) zircon saturation conditions, although
620 Watson and Harrison (1983) conditions can be easily implemented if preferred. Crystal sizes
621 range from 49 to 60 μm and M-factor of the melt is assumed to be a function of the temperature
622 per Bindeman and Melnik (2016) formulation. As was shown in the latter paper, consideration of
623 compositional effects (M-factor) typically results in faster zircon dissolution and growth during
624 temperature oscillations. Furthermore, we allow for change in zircon cell size caused by
625 crystallization of other minerals on the zircon cell's boundary. This promotes faster zircon
626 growth during cooling, and faster zircon dissolution during country rock melting.
627 We additionally consider cells with different bulk Zr concentration (Fig. 9) ranging from
628 50 to 150 ppm. While concentrations of <~80 ppm are least realistic for igneous rocks, as is
629 described in Bindeman and Melnik (2016) metamorphic and intraplutonic recrystallization may
630 lead to areas within a rock with strongly different Zr concentration. For example, zircon may be
631 surrounded by Zr-poor quartz-feldspar assemblage that will melt as cotectic during temperature
632 increase. Survivability of zircons is, thus, strongly depends on the zircon size and its cell size
633 defining total Zr concentration within a cell. All the crystals in current model will grow to the
634 same size governed by bulk zirconium concentration if the temperature returns to the same value.
635
636 Below we consider several scenarios of zircon behavior. For crustal rock particle close to the
637 center of the intrusion, as the temperature increases due to continues magma supply, zircon

dissolution begins. In the case of a large initial crystal (60 μm sitting in a cell of with and large C_{bulk}= 150 ppm Zr) only small portion of the crystal dissolves (red solid curve), while for C_{bulk} = 25 zircon dissolves completely and restarts the growth when the temperature drops down to saturation conditions. In this case the crystal will be significantly younger.

Inside of the intruded magma, zircon crystallize as soon as the temperature drops below saturation temperature and crystallizes until the solidus (initially) or until the thermal equilibration with the main reservoir. In the case of late injection, the initial temperatures in the beginning are too high and magma remains Zr undersaturated until the whole magma body temperature drops below zircon saturation after cessation of new magma addition. Expectedly, for smaller bulk Zr concentrations (C_{bulk}), magma saturation with zircon occurs at lower temperatures and zircon age is much younger than for large C_{bulk}. For Zr-richer magmas zircon growth will start immediately after the injection.

As our 2D models permits simultaneous computation of destinies in 50000 of magmatic zircons, we can describe evolution of zircon age patterns in the entire magma body. Fig. 10 shows the distribution of growth durations (final time - starting time) of these 50000 magmatic zircons, which demonstrate important spatial and temporal complexity. As dikes cool and crystallize quickly without a subsequent episode of remelting in the periphery of the intrusion, zircons grow for years to tens of years and the age distribution between the core and the rim is very restricted and is identical to that of the country rock or that of the intruded dike.

Spatially, in the central part of the intrusion, newly accumulated melts crystallize and continue to cool down much slower and zircons record continuous growth of hundreds ka, with rims of these crystals younger than their cores by this exact amount of time. Zircon core age-relationships can be a diagnostic criterion of the magma parcels location within the intrusion, and the mechanism of the intrusion formation. A great number of zircons record periods of dissolution, then growth, the intensity of which depends on the proximity to the intruded dikes. In studying plutonic rocks, this may be a tool to investigate spatial distribution. However, in the case when the boundaries between individual zones inside of the plutons are blended (cf Bartley et al. 2020), random sampling of an accreted intrusion may just record a particular episode of local zircon crystallization.

669

670 Temporally, early eruptions from the growing magmatic system will expectedly sample ages of
671 these individual intrusions and not the country rocks, which have not yet melted. At intermediate
672 stages of intrusion development (Fig. 3), formed magmas will sample zircons from country rocks
673 providing a great deal of inherited zircons diversity ranging in age from country rocks to time of
674 the intrusion. Some magma system at low flux rates will end up in this situation.

675

676 Among 12800 markers related to host rock parcels only half (~ 6390) experienced certain degree
677 of melting. The rest of the rocks were displaced by dike injection far from high temperature
678 region and were not altered by the magma intrusion. Fig. 11 shows the distribution of the zircons
679 that experienced dissolution and therefore rejuvenation of the average zircon age reduction (a)
680 and the histogram of the volume fraction of preserved cores (b) for the initial zircon radius of
681 100 μm. In the central area of the intrusion ~ 5% zircons associated with host rocks were totally
682 melted and later grew again, therefore, the age of zircons erupted from this region will be totally
683 controlled by magma intrusion time. Due to high special heterogeneity of the central part of the
684 intrusion some of the host rocks zircons remain unaltered in the central part of the intrusion.
685 There is a spectrum of average zircon ages in a single magma blob that can complicate the
686 interpretation of the history of particular magmatic chamber. The proportion of magmatic to
687 host-rock zircons that can be erupted depends on the degree of melting and temperature-time
688 histories for particular locations, and these are explored more below by assigning specific O and
689 Hf isotopic values to magma and areas in the crust.

690 Zircon destinies will strongly depend on the overall magma flux Q and magma focusing
691 W. Defocused systems with low magma flux will generate and preserve great deal of zircon age
692 diversity and inherited cores. Notice that the majority of cores will not be from country rocks but
693 rather from earlier crystallized intrusions (80-90%, Fig. 7), thus recording the earliest episodes of
694 magma intrusion. However, at large magma flux rate, most initially crystallized and most
695 country-rock zircons (except the ones at the periphery) will dissolve.

696 The main conclusion of the current 2D model are that high flux and focused systems lead
697 to rejuvenation of most zircon ages and maintaining strong core-rim heterogeneity between the
698 core and the rim of the intrusion as a whole. If only the magma stored in the center of intrusion is
699 allowed to erupt (thus sampling the main body of the growing magma) only “eruption age”

zircons will be observed. These are predicted to have a long tail of ages going back to the beginning of zircon crystallization, which as we demonstrate here may be as long as a few tens-hundred ka. The fact that many erupted zircons from large supervolcanic systems such as Bishop Tuff and Yellowstone do not have such long tails (Crowley et al. 2007; Wotzlaw et al. 2015) and most zircons are of eruption age (±5-10ky) signals that magma system was not allowed to age before eruption, and magmas were erupted soon after formation. Such relationships signify an important difference between such volcanic and mush-dominated (Fish Canyon tuff, with zircon age tails of 300 ka, Wotzlaw et al. 2013) and plutonic environments, where zircons can span 10 My (Glazner et al. 2004).

It is also important to note that sporadic magma injection during the cooling stage of the already formed magma body leads to small amplitude thermal spikes due to the overall high thermal inertia of the system, resulting in short-lived episodes of zircon dissolution. We earlier modelled that oscillatory zoning in zircons can be formed this way (Melnik and Bindeman, 2018).

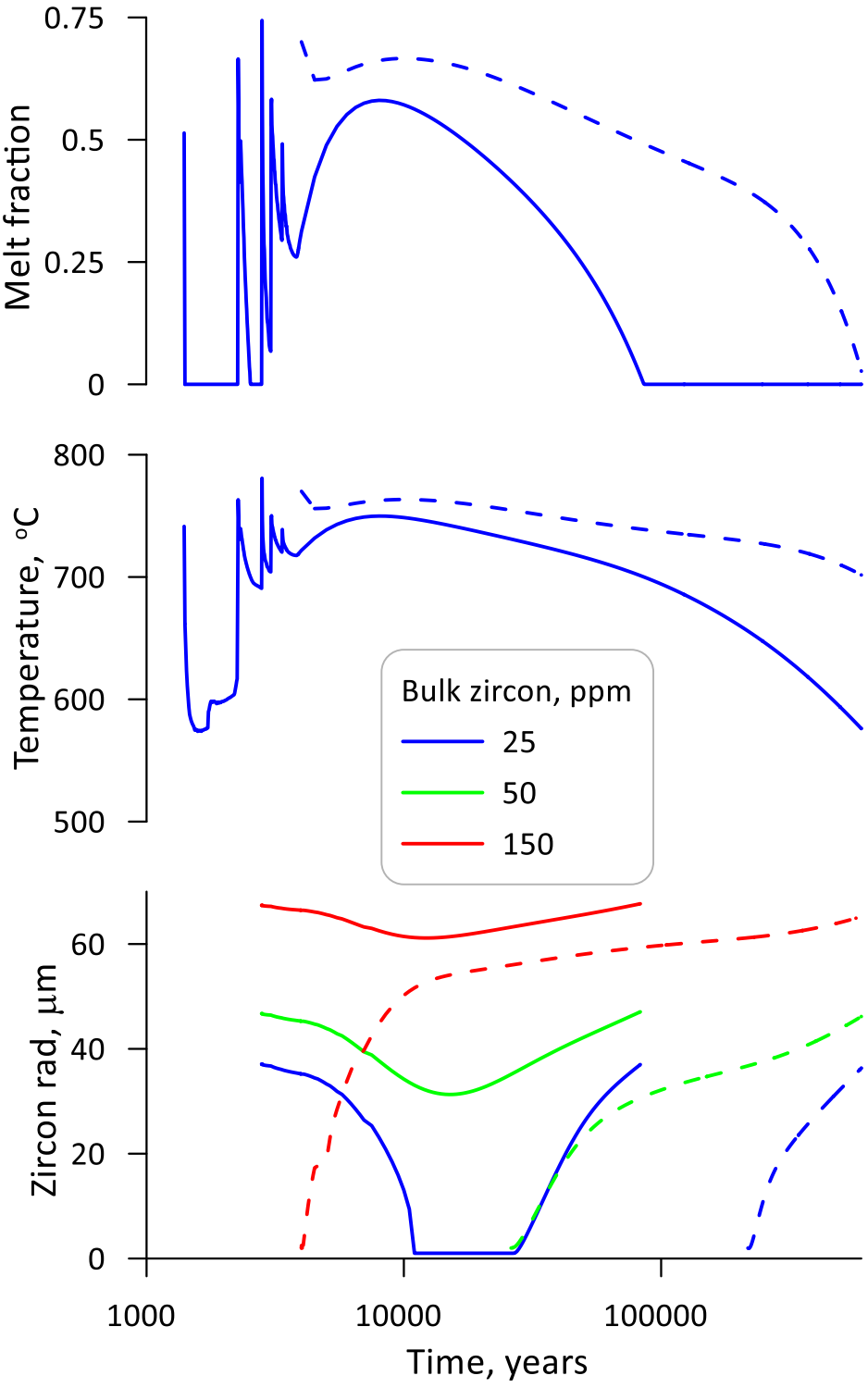

Figure 9. Evolution of the melt fraction (up), temperature (middle) and zircon radius (bottom) recorded in two magma parcels, surrounded by rock with Different bulk zirconium contents in magma are shown by colors. Notice that zircons in Zr-poor rocks will get completely dissolved,

then regrown, while zircons in Zr-richer rocks will undergo only partial dissolution, developing structure of inherited core surrounded by a rim

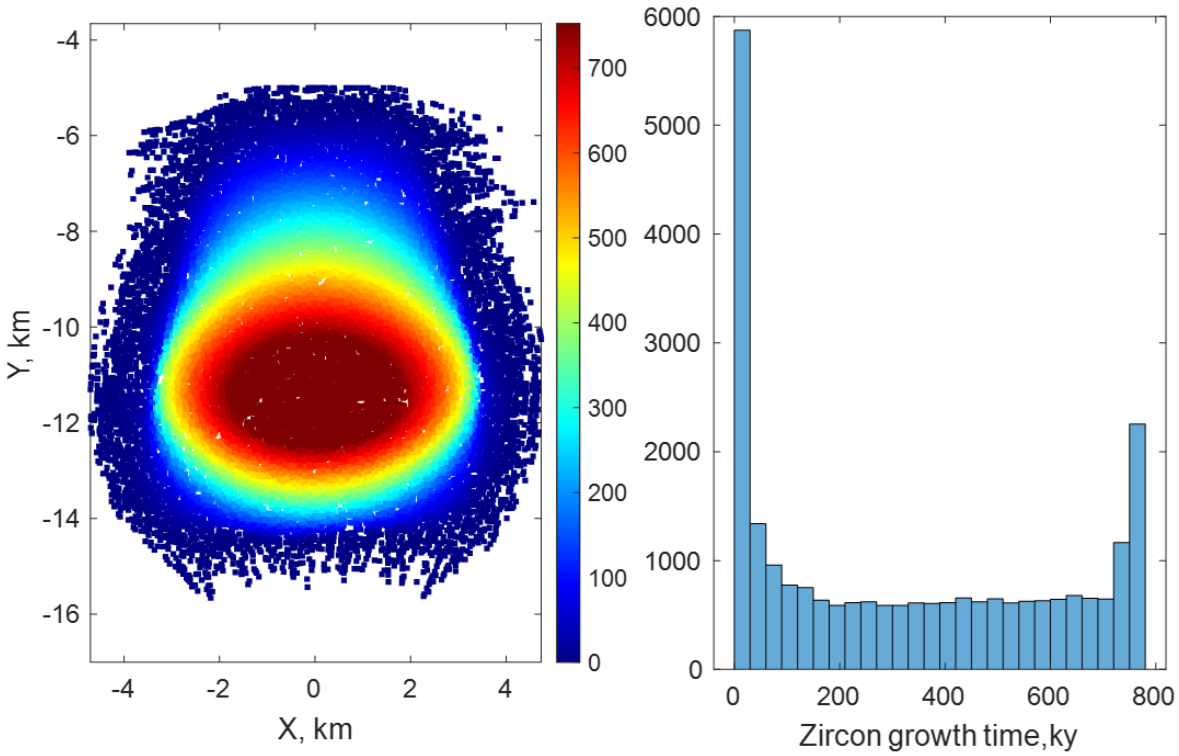

Figure10. Distribution of the growth time of magmatic zircons within the intrusion, corresponding to case Q=1 m^3/s L=4 km in Fig. 3. Notice distinctly concentric structure due to completely molten core of the intrusion. Zircons near intrusion edges retain great diversity of ages shown in B.

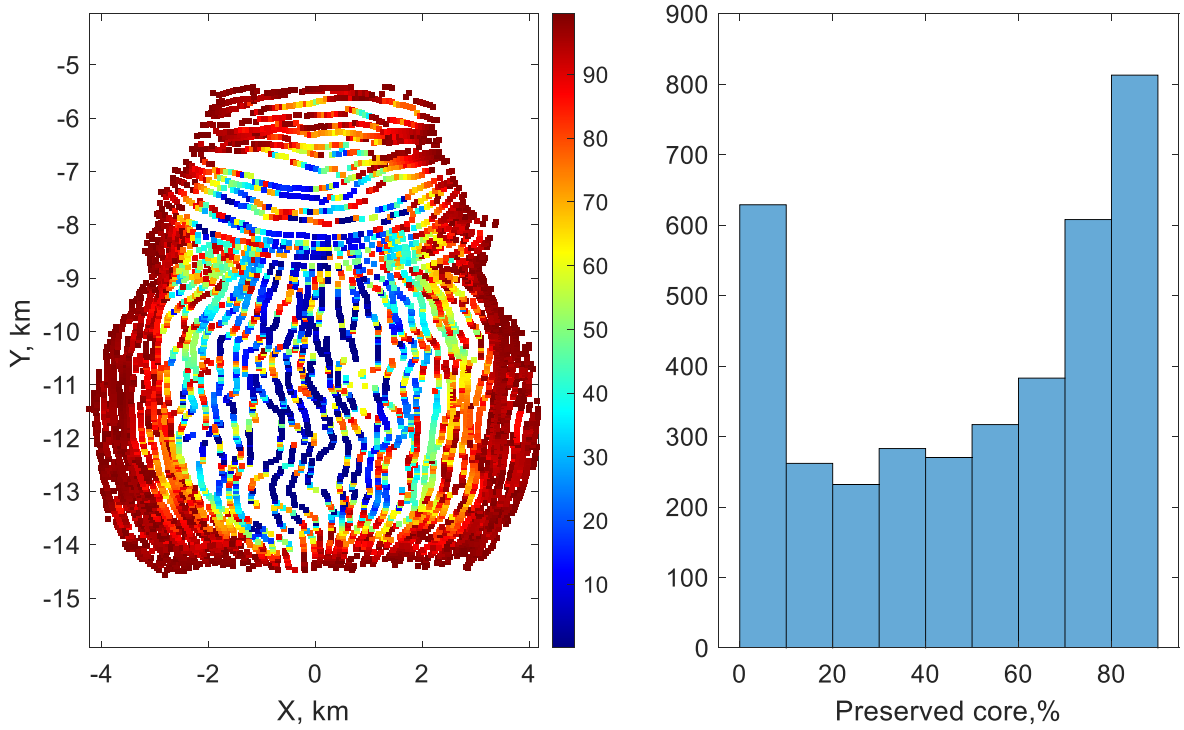

Figure 11. Distribution of zircon core preservation in country rocks affected by dike intrusions. (a) Notice that rind of the intrusions preserves the original zircons without much dissolution because these formed early in thermal history, when country rocks were cold; these areas were displaced to the sides by subsequent intrusions. The core of the intrusion preserves diverse cores. (b) Number of zircon cores plotted for % preservation.

3.5. Hf and O isotope distribution

Fig 12 considers distribution of oxygen and Hf isotope inside of the growing magma body, which tracks down percentage of crustal and mantle-magma (Hf isotopes) and % of crustal, mantle, and hydrothermally altered country rocks involved in intrusion formation. As our model does not allow magma movement, this modeling signifies potential for naturally generating isotopic heterogeneities in different areas of the growing magma body. In this sense each 500x500 m zone will have parcels (batches of melt) that can locally mix (and crystallize zircons with distinct O and Hf isotopes) in proportion to melts from the above mentioned crustal and mantle-derived rock parcels. Should these magma batches allowed to further mix along the laterally and vertically interconnected network of magmatic column of eruptible magma (e.g.,

Cashman et al. 2017), such eruption will likely preserve these diversity in the eruptive products, similar to what is observed in many supervolcanic eruptions of the Yellowstone plume (Bindeman and Simakin, 2014; Wotzlaw et al 2014; 2015).

However, if such system were not allowed to erupt but are allowed to internally convect over many hundreds of thousands of years in a semi-mushy state, periodically activated by intrusions, this should generate a more homogenous mix of diverse zircons within a single hand specimen.

Aging inside of plutons may further anneal isotopic differences, resulting in relatively homogenous (with respect to O and Hf isotopes) magma parcels, which still record long zircon crystallization tails.

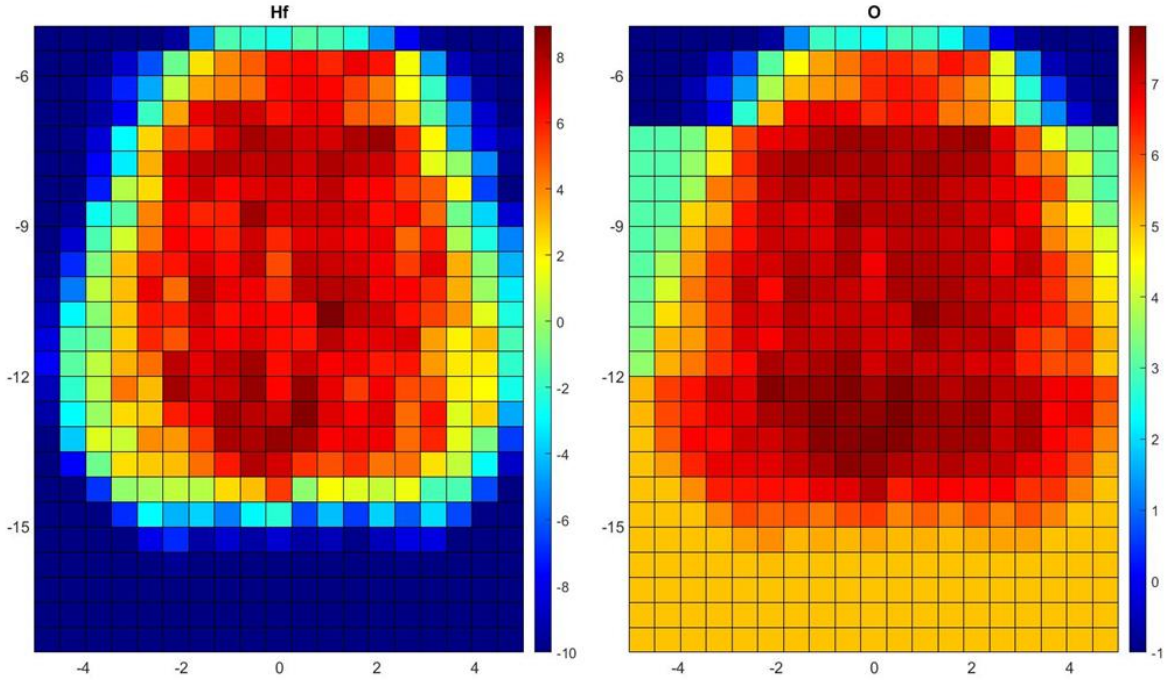

Figure 12. Distribution of Hf and O isotopes averaged in 500x500 m grid. Magma Hf +10, O +8

4 Discussion

Formation of crustal magmatic systems involves magma injection from depth, heat and mass transfer, melt and gas separation and episodic volcanic eruption (e.g., McBirney, 2006). It is obvious that no single model can capture complexity of these diverse processes, that requires solution of conjugate fluid-solid-heat problem coupled with and chemical problem (phased

767 diagram, rock compositions). Previously widely applied 1D or 2D cylindrical magma chambers
768 models with underplating (Annen and Sparks, 2002; Dufek and Bergantz, 2005; Annen et al.
769 2006, Caricchi et al. 2014; 2016) lead to the development of quantitative intuition of our
770 understanding of the relationship of the magma flux rates and melting efficiencies at different
771 geotherms and depths. In all current models, a simple kinematics is prescribed, as the whole
772 crustal column with previously intruded sills is moving vertically down upon emplacement of
773 each additional sill intrusion, or horizontally sideways upon intrusion of a dike.

774 Previously proposed and widely utilized magma body formation by relying on axisymmetric
775 geometries of intrusion with prescribed position of magma injections and rock associated
776 displacements taught us important first-order trends in magma body formation and evolution.
777 The model and software presented in this paper a new model of 2D magma chamber formation
778 by dike and sill injection and this that allows us and potential users to investigate spatio-temporal
779 details of magma body growth and evolution, including zircon histories. Furthermore, we
780 simulated elastic response to dike and sill injection, realized via spreading of markers which
781 creates accommodation for new intrusions by moving them apart. Incorporation of realistic
782 displacements in the 2D model makes a dramatic difference in the evolution of the temperature
783 field, and melt production, and melt distribution (Fig. 3). We believe that our model provide a
784 realistic and high-resolution description of thermal, compositional, and melt % distribution
785 without relying on prescribed whole-system behaviors.

786 After formation of large and interconnected melt regions, thermal and compositional convection
787 can significantly intensify heat transfer, but this process is not currently considered in this model,
788 or previously published thermal-elastic models. In nature, unmolten rock screens surrounded by
789 magma would likely sink leading to segregation of melt, and magma in large melt fraction areas
790 in between cohesive solid framework would flow. Instead, our model assumes possibility of dike
791 penetration through areas that are >60% molten. Similar behavior is accepted in previously
792 proposed models of Annen et al. (2006), Annen (2009) and Caricchi et al. (2016), especially
793 those including intraplating and overplating. In a certain way, the lack of internal segregation in
794 these models is compensated by the possibility of internal diking, balancing the overall heat and
795 mass balance. While this may appear as locally physically unrealistic, delivery of magma
796 through a melt layer may instead proceed via magma addition, magma mixing and convective

advection of heat and mass. The latter have similar overall effect on the thermal evolution of the system as a whole, especially in its central fully molten part. Segregation and magma mixing processes will homogenize melt fractions and temperatures to a greater degree than is shown, while global % melt and temperature evolution will remain similar.

The bulleted points below outline broad implications of our new model to magma body formation in nature.

1) As expected, magma flux controls the efficiency of magma production via melt accumulation and country rock melting. Equally important is melt focusing, which depends on the width of the injection region. Magma injection with the low discharge rate, or in a wide region, can produce no eruptible melt, while significant volume of melt forms for focused dike emplacement. At higher discharge rates the melt production efficiency increases but the influence of the domain size remains significant.
2) The model predicts temperature-time histories of melts formed by crystallization and partial melting of host rocks. We observe highly non-monotonic temperature distributions in space and time, especially in the beginning of magma chamber formation that corresponds to individual dike emplacements into the cold crust. Formation of the significant volume of molten magma later in the course buffers temperature oscillations, leading to "McBirney-type" liquid core magma body.
3) Depending on the magma flux, melt focusing generates fully molten cores filled with liquidus magma and surrounded by thick "mushified" rinds and partial melt as predicted for "classic" drawings of textbook magma chambers (McBirney, 2006; Marsh, 1981). Defocused systems, and systems with low flux, generate much less melt and such systems may cool as plutons (e.g., Glazner et al. 2004), and subsequently exhibit a variety of observed intraplutonic processes of mass-redistribution (Bartley et al. 2020) initial stages of which can be understood via our model of randomized dike intrusion.
4) Ordinary magma flux rates comparable to those observed in island arcs are capable of rapid generation of large, 10^2 km^3 volumes of silicic melt over ~$4x10^3$ years, especially if this magma injection is focused in a relatively narrow zone, and mostly due to accumulation of such melts.
5) The magma system that is getting formed reminds network of dikes, sills and magma bodies interconnected over large vertical domains in the crust. Such systems are able to

provide high silicic magmas discharge rates in the course of supervolcanic eruptions (Sparks et al. 2017) or voluminous Yellowstone lava flows (Loewen et al. 2017).

6) Mapping of zones of melt with >50% melt in the model demonstrates that these are distributed in a tortuous pattern with a great deal of both vertical and lateral interconnectivity. Such configuration would enable easy flow of magma averaging out regional heterogeneities on magma flow timescales.
7) Melting by basalts or andesites vs melting by hot rhyolites (including addition of rhyolites from below) has surprising similarities in the total volume of generated melt (Fig. 7).

Our new model is tested to its ability to generate a) crustal melt and b) total melt, and describes melt volume-time histories of such melts during the growth of the intrusion, and its subsequent cooling. Points below outline specific implications for our model with respect to crustal melting.

1) An important and previously unexplored result is in our 2D model is that simulated rock spreading and heat propagation leads to less efficient crustal melting. During the initial stages of intrusion (crustal preconditioning) magma is capable of melting only up to 15-20% of the ambient crust. Subsequent intrusion will have to melt this already diluted crust-dike (e.g. "crust-mantle") mixtures. Furthermore, after the establishing the partial rind zone with 30% crustal melt, subsequent magmatism is dominated chemically and isotopically by the intruded dikes. This result is in line with observations that even in the hot-spot related examples of magmatism, such as Iceland or the Snake River Plain, where high temperature mantle-derived Yellowstone-plume magmas intrude the Archean crust, they assimilate at most 10-20% of such crust based on Nd-crustal index (Nash et al. 2006), and based on earlier reported results of crust-wide thermomechanical modeling (e.g. Colón et al. 2019). Therefore, the high-resolution model in this paper provides a more realistic estimates of maximum possible extent of crustal melting by dike and sills intrusion.
2) We thus revise downward the maximum possible "melting efficiency" from previously published models, even though our model includes hot liquidus magmas. The undoubted presence of high-degree or pure crustal melts in the geologic record, commonly with a highly peraluminous nature (Bucholz et al. 2018) negates their generation by dike

858 intrusion and must be related to radioactive heating (migmatization and assembly) at
859 deep crustal zones.
860 3) The model also predicts lateral and vertical heterogeneities, due to naturally-generated
861 crustal melts vs newly injected melt, for both the rhyolitic intrusions and andesitic
862 intrusion cases. It identifies areas with >50% melt, potentially eruptible magma, which
863 contain variable proportions of crustal melt vs original melt. In nature this would
864 correspond to a) varying isotopic composition b) variable proportion of inherited zircons
865 c) in the case of andesitic partial melt-silicic remelt, various bulk melt compositions.
866
867 Integration of computed thermal and melting histories with zircon crystallization software
868 allows us to predict zircon dissolution/crystallization conditions in 25,000 markers across the
869 model (Fig. 11) and the dissolution/overgrowth destinies of inherited zircons. Such modeling
870 helps in understanding zircon record in magmatic rocks that range from extremely diverse to
871 extremely homogeneous with respect to age. Examples of extremely diverse zircon record
872 include small magmatic systems such as Mt St Helens (Claiborne et al. 2010a); and large size
873 systems such as Peach Spring (Claiborne et al. 2010b) and the Fish Canyon Tuffs (Wotzlaw
874 et al. 2013). Examples of very homogeneous with respect to age, but very diverse with
875 respect to crust/mantle proportion (diverse O and Hf isotopes) systems include most of
876 Yellowstone hotspot track magmas (Bindeman and Simakin, 2014; Wotzlaw et al. 2014,
877 2015). The bulleted points below outline specific results of our modeling.
878 1) Complex zircon growth patterns occur in the beginning of the magma chamber
879 formation with several episodes of complete or partial dissolution and regrowth.
880 Early injected dikes will cool quickly and stay in the periphery of the forming
881 magma chamber resulting in very restricted ages of zircons corresponding to active
882 diking period.
883 2) At early stages of magma body formation, and later around its periphery, both host
884 rock and magmatic zircons will show a variety of ages and age distribution between
885 cores and rims. Most of host-rock zircons are shifted towards the periphery of the
886 growing magma body, which experience only partial melting followed by further
887 regrowth.

3) Zircons in the central part of the intrusion are mostly fully dissolved and reprecipitated, leaving no inherited core. Only small portion of the intrusion keeps some part of an old core.
4) Zircons grow and age together with magma cooling and crystallization and thus rim age corresponding to the cooling interval of the intrusion, unless it is interrupted by the eruption of magma. Thus, crystals in the center of the intrusion will have a long growth history spanning a few 100 ky age difference between the core and the rim. This concentric age zoning must be taken into account during interpretation of large volume ignimbrites or plutonic rocks.
5) Melting by hotter magmas (basalts and andesites) should lead to more aggressive reset of zircons especially in the central parts of the intrusion due to higher T and M factors; however lateral intrusion heterogeneity and zircon diversity in age and O and H isotopes will persist.
6) When % of crustal melt vs dike melt is translated into crustal-mantle O and Hf isotopic end-member values (e.g. Fig. 12) in the whole system, and in areas with >50% melt across the system, we observe natural development of diversity of O and Hf isotopes in different areas within the system.
7) Depending on the magma flux and melt focusing two end-member scenarios are possible for zircon record.
8) At low magma fluxes and melt defocusing, zirconal record reminds “Fish Canyon type” (Wotzlaw et al. 2013) when large volume of crystal-rich rhyodacitic magmas with 40-45% crystals inherited from variable crust-mantle mixtures, favoring the crust. Many zircons got inherited tailing back to many hundreds of thousands of years signifying long mush residence in the crust (Bachmann et al. 2002). Each hand specimen contains crystals delivered from isotopically diverse (e.g. O and Hf) country rocks including Archean basement. Observed high level of inheritance suggests that incorporated magma volumes were not fully molten. Each hand specimen represents a heterogeneous mixture of these; while laterally, bulk chemical composition is “monotonous intermediate” homogenous mix, suggesting effective remobilization of >50% melt fractions with suspended convection of crystal-melt mixtures.

i) At high magma flux and melt focusing, zirconal record becomes "Yellowstone" type (Bindeman and Simakin, 2014; Wotzlaw et al. 2014; 2015) when large volumes of near liquidus, crystal poor magmas are erupted. These exhibit zircons of identical age, within time-resolution of ±500-1000years using the best geochronological methods available CA-ID-TIMS. however, they exhibit extreme diversity of crust/mantle proportions (via O and Hf isotopes in zircons) suggesting that magmas were generated simultaneously in different parts of the fully molten system but with different proportions of crust/mantle there, and erupted without delay. These observations suggest that pockets of melt with highly diverse crust-mantle proportions got rapidly heated above zircon saturation, zeroing the ages, followed by zircon crystallization in the same isolated pockets. This was followed by a rapid assembly of such pockets and eruption. Time between crystallization of zircons is <~5000years.

Acknowledgments, Samples, and Data

This paper is dedicated to Alexander R. McBirney (1924-2019) a prominent volcanologist and a founder of the University of Oregon Volcanology Program, the first in the country. IB and OM thank RNF Grant (grant RNF19-17-00241) for support, IU thanks RFBR Grant #18-01-00352 for partial financial support, Meredith Townsend for pre-review comments. This paper is a theoretical work and does not contain new data.

Executable file, example, user manual and selected temperature histories from Fig. 8 are available from the repository Melnik, Oleg; Utkin, Ivan ; Bindeman, llya (2020), "Supplementary material for JGR paper "Magma chamber formation by dike accretion and crustal melting: 2D thermal model with emphasis on zircon record"", Mendeley Data, V1, doi: 10.17632/88jmjgj7zy.1.

945 **References**

946 Annen, C. (2009). From plutons to magma chambers: Thermal constraints on the accumulation
947 of eruptible silicic magma in the upper crust. Earth and Planetary Science Letters.
948 https://doi.org/10.1016/j.epsl.2009.05.006

949 Annen, C., & Sparks, R. S. J. (2002). Effects of repetitive emplacement of basaltic intrusions on
950 thermal evolution and melt generation in the crust. *Earth and Planetary Science*
951 *Letters*, *203*(3-4), 937-955. https://doi.org/10.1016/S0012-821X(02)00929-9

952 Annen, C., Blundy, J.D., Sparks, R. S. J. (2006) The genesis of intermediate and silicic magmas
953 in deep crustal hot zones. Journal of Petrology 47 (3), 505-539

954 Andrews, B. J., & Befus, K. S. (2020). Supersaturation Nucleation and Growth of Plagioclase: a
955 numerical model of decompression-induced crystallization. Contributions to Mineralogy
956 and Petrology. https://doi.org/10.1007/s00410-020-1660-9

957 Bachmann, O., Dungan, M. A. & Lipman, P. W. (2002). The Fish Canyon magma body, San
958 Juan volcanic field, Colorado: Rejuvenation and eruption of an upper crustal batholith.
959 Journal of Petrology 43, 1469–1503.

960 Barnett, Z. A., & Gudmundsson, A. (2014). Numerical modelling of dikes deflected into sills to
961 form a magma chamber. *Journal of Volcanology and Geothermal Research*.
962 https://doi.org/10.1016/j.jvolgeores.2014.05.018

963 Bartley, J. M., Glazner, A. F., Stearns, M. A., & Coleman, D. S. (2020). The granite aqueduct
964 and autometamorphism of plutons. *Geosciences (Switzerland)*.
965 https://doi.org/10.3390/geosciences10040136

966 Becerril, L., Galindo, I., Gudmundsson, A. et al. (2013) Depth of origin of magma in eruptions.
967 Sci Rep 3, 2762. https://doi.org/10.1038/srep02762

968 Biggs, J., & Annen, C. (2019). The lateral growth and coalesence of magma systems.
969 *Philosophical Transactions of the Royal Society A: Mathematical, Physical and*
970 *Engineering Sciences*. https://doi.org/10.1098/rsta.2018.0005

971 Bindeman, I. N., & Melnik, O. E. (2016). Zircon survival, rebirth and recycling during crustal

melting, magma crystallization, and mixing based on numerical modelling. *Journal of Petrology*. https://doi.org/10.1093/petrology/egw013

Bindeman I.N., Simakin, A.G. (2014) Rhyolites—Hard to produce, but easy to recycle and sequester: Integrating microgeochemical observations and numerical models. Geosphere 10 (5), 930-957

Brackbill, J. U., & Ruppel, H. M. (1986). FLIP: A method for adaptively zoned, particle-in-cell calculations of fluid flows in two dimensions. *Journal of Computational physics*, *65*(2), 314-343. https://doi.org/10.1016/0021-9991(86)90211-1

Bryan, S., Ernst R, (2007). Proposed Revision to Large Igneous Province Classification. Earth-Science Reviews. 86 (1): 175–202.

Bucholz, C. E., Stolper, E. M., Eiler, J. M., & Breaks, F. W. (2018). A comparison of oxygen fugacities of strongly peraluminous granites across the Archean–Proterozoic boundary. *Journal of Petrology*, *59*(11), 2123-2156. https://doi.org/10.1093/petrology/egy091

Caricchi, L., Annen, C., Blundy, J., Simpson, G., & Pinel, V. (2014). Frequency and magnitude of volcanic eruptions controlled by magma injection and buoyancy. *Nature Geoscience*. https://doi.org/10.1038/ngeo2041

Caricchi, L., Simpson, G., & Schaltegger, U. (2014). Zircons reveal magma fluxes in the Earth' s crust. *Nature*. https://doi.org/10.1038/nature13532

Caricchi, L., Simpson, G., & Schaltegger, U. (2016). Estimates of volume and magma input in crustal magmatic systems from zircon geochronology: The effect of modeling assumptions and system variables. *Frontiers in Earth Science*. https://doi.org/10.3389/feart.2016.00048

Cashman, K. V., Sparks, R. S. J., & Blundy, J. D. (2017). Vertically extensive and unstable magmatic systems: A unified view of igneous processes. *Science*. https://doi.org/10.1126/science.aag3055

Claiborne, L. L., Miller, C. F., Gualda, G. A., Carley, T. L., Covey, A. K., Wooden, J. L., & Fleming, M. A. (2018). Zircon as magma monitor: Robust, temperature-dependent partition coefficients from glass and zircon surface and rim measurements from natural

systems. *Microstructural geochronology: Planetary records down to atom scale*, 1-33. https://doi.org/10.1002/9781119227250.ch1

Claiborne, L. L., Miller, C. F., Flanagan, D. M., Clynne, M. A., & Wooden, J. L. (2010). Zircon reveals protracted magma storage and recycling beneath Mount St. Helens. Geology. https://doi.org/10.1130/G31285.1

Claiborne, L. L., Miller, C. F., & Wooden, J. L. (2010b). Trace element composition of igneous zircon: a thermal and compositional record of the accumulation and evolution of a large silicic batholith, Spirit Mountain, Nevada. *Contributions to Mineralogy and Petrology*, *160*(4), 511-531. https://doi.org/10.1007/s00410-010-0491-5

Colón D.P., Bindeman I.N., Gerya T.V. (2019) Understanding the isotopic and chemical evolution of Yellowstone hot spot magmatism using magmatic-thermomechanical modeling. Journal of Volcanology and Geothermal Research 370, 13-30

Colón D.P., Bindeman I.N., Gerya T.V. (2018) Thermomechanical modeling of the formation of a multilevel, crustal-scale magmatic system by the Yellowstone plume. Geophysical Research Letters 45 (9), 3873-3879

Costa, F., Dohmen, R., Chakraborty, S. (2008) Time scales of magmatic processes from modeling the zoning patterns of crystals. Reviews in Mineralogy and Geochemistry 69 (1), 545-594

Crowley, J. L., Schoene, B., & Bowring, S. A. (2007). U-Pb dating of zircon in the Bishop Tuff at the millennial scale. *Geology*, *35*(12), 1123-1126. https://doi.org/10.1130/G24017A.1

DePaolo, D.J., Harrison, T.M., Wielicki, M., Zhao, Z., Zhu, D.C., Zhang, H, Mo, X. (2019) Geochemical evidence for thin syn-collision crust and major crustal thickening between 45 and 32 Ma at the southern margin of Tibet. Gondwana Research 73, 123-135.

Dufek, J., & Bergantz, G. W. (2005). Lower crustal magma genesis and preservation: a stochastic framework for the evaluation of basalt–crust interaction. *Journal of Petrology*, *46*(11), 2167-2195. https://doi.org/10.1093/petrology/egi049

Edmonds M., Cashman K.V., Holness M., Jackson M. (2019) Architecture and dynamics of magma reservoirs. *Philosophical Transactions of the Royal Society A Mathematical*,

Physical and Engineering Sciences. 377(2139):20180298. https://doi.org/10.1098/rsta.2018.0298

Elsworth, D., Foroozan, R., Taron, J., Mattioli, G. S., & Voight, B. (2014). Geodetic imaging of magma migration at Soufrière Hills Volcano 1995 to 2008. *Geological Society, London, Memoirs, 39*(1), 219-227. https://doi.org/10.1144/M39.12

Gerya, T.V., Yuen, D.A., 2003. Characteristics-based marker-in-cell method with conservative finite-differences schemes for modeling geological flows with strongly variable transport properties. Phys. Earth Planet. Inter. 140, 293–318. https://doi.org/ 10.1016/j.pepi.2003.09.006.

Glazner A.F., Bartley J.M., Coleman D.S., Gray W., Taylor R.Z. (2004) Are plutons assembled over millions of years by amalgamation from small magma chambers? GSA today 14 (4/5), 4-12

Gudmundsson, A., Lecoeur, N., Mohajeri, N., & Thordarson, T. (2014). Dike emplacement at Bardarbunga, Iceland, induces unusual stress changes, caldera deformation, and earthquakes. *Bulletin of Volcanology*, *76*(10), 869. https://doi.org/10.1007/s00445-014-0869-8

Heath, B.A., Hooft, E.E.E., Toomey, D.R. (2018) Autocorrelation of the seismic wavefield at Newberry Volcano: Reflections from the magmatic and geothermal systems. Geophysical Research Letters 45 (5), 2311-2318

Huber, C., Parmigiani A. (2018) A physical model for three-phase compaction in silicic magma reservoirs. Journal of Geophysical Research: Solid Earth 123 (4), 2685-2705

Huber, C., Townsend, M., Degruyter, W., Bachmann, O. (2017) Optimal depth of subvolcanic magma chamber growth controlled by volatiles and crust rheology. Nature Geoscience 12 (9), 762-768

Huppert, H., & Sparks, R. S. J. (1988). The generation of granitic magmas by intrusion of basalt into continental crust. *Journal of Petrology*, *29*(3), 599-624. https://doi.org/10.1093/petrology/29.3.599

Karakas, O., Degruyter, W., Bachmann, O., & Dufek, J. (2017). Lifetime and size of shallow magma bodies controlled by crustal-scale magmatism. *Nature Geoscience*.

https://doi.org/10.1038/ngeo2959

Krumbholz, M., Hieronymus, C. F., Burchardt, S., Troll, V. R., Tanner, D. C., & Friese, N. (2014). Weibull-distributed dike thickness reflects probabilistic character of host-rock strength. *Nature Communications*. https://doi.org/10.1038/ncomms4272

Lensky, N. G., Niebo, R. W., Holloway, J. R., Lyakhovsky, V., & Navon, O. (2006). Bubble nucleation as a trigger for xenolith entrapment in mantle melts. *Earth and Planetary Science Letters*, *245*(1-2), 278-288. https://doi.org/10.1016/j.epsl.2005.11.064

Loewen, M.W., Bindeman, I.N., OE Melnik, O.E. (2017) Eruption mechanisms and short duration of large rhyolitic lava flows of Yellowstone. Earth and Planetary Science Letters 458, 80-91

Marsh, B. D. (1981). On the crystallinity, probability of occurrence, and rheology of lava and magma. *Contributions to Mineralogy and Petrology*, *78*(1), 85-98. https://doi.org/10.1007/BF00371146

McBirney, A.R. (2006) Igneous Petrology. Jones & Bartlett Learning, 550 p

Melnik, O. E., & Bindeman, I. N. (2018). Modeling of trace elemental zoning patterns in accessory minerals with emphasis on the origin of micrometer-scale oscillatory zoning in zircon. *American Mineralogist: Journal of Earth and Planetary Materials*, *103*(3), 355-368. https://doi.org/10.2138/am-2018-6182

Menand, T., Daniels, K. A., & Benghiat, P. (2010). Dyke propagation and sill formation in a compressive tectonic environment. *Journal of Geophysical Research: Solid Earth*, *115*(B8). https://doi.org/10.1029/2009JB006791

Miller, C. F., Furbish, D. J., Walker, B. A., Claiborne, L. L., Koteas, G. C., Bleick, H. A., & Miller, J. S. (2011). Growth of plutons by incremental emplacement of sheets in crystal-rich host: Evidence from Miocene intrusions of the Colorado River region, Nevada, USA. *Tectonophysics*, *500*(1-4), 65-77. https://doi.org/10.1016/j.tecto.2009.07.011

Muskhelishvili, N. I. (1977). Basic Equations of the Plane Theory of Elasticity. In *Some Basic Problems of the Mathematical Theory of Elasticity*. https://doi.org/10.1007/978-94-017-3034-1_4

1086 Papale, P. Global time-size distribution of volcanic eruptions on Earth. Sci Rep 8, 6838 (2018).
1087 https://doi.org/10.1038/s41598-018-25286-y

1088 Patankar, S. (1980). Numerical Heat Transfer and Fluid Flow. Boca Raton: CRC Press,
1089 https://doi.org/10.1201/9781482234213

1090 Robinson, J. E., & Eakins, B. W. (2006). Calculated volumes of individual shield volcanoes at
1091 the young end of the Hawaiian Ridge. *Journal of Volcanology and Geothermal Research*.
1092 https://doi.org/10.1016/j.jvolgeores.2005.07.033

1093 Rubin, A. M. (1995). Propagation of magma-filled cracks. *Annual Review of Earth & Planetary*
1094 *Sciences*. https://doi.org/10.1146/annurev.ea.23.050195.001443

1095 Schöpa, A., Annen, C., Dilles, J. H., Sparks, R. S. J., & Blundy, J. D. (2017). Magma
1096 emplacement rates and porphyry copper deposits: Thermal modeling of the yerington
1097 batholith, Nevada. *Economic Geology*. https://doi.org/10.5382/econgeo.2017.4525

1098 Schaltegger, U., Nowak, A., Ulianov, A., Fisher, C. M., Gerdes, A., Spikings, R. et al. (2019).
1099 Zircon Petrochronology and $^{40}Ar/^{39}Ar$ Thermochronology of the Adamello Intrusive
1100 Suite, N. Italy: Monitoring the Growth and Decay of an Incrementally Assembled
1101 Magmatic System. *Journal of Petrology*, *60*(4), 701-722.
1102 https://doi.org/10.1093/petrology/egz010

1103 Simakin, A., & Talbot, C. (2001). Tectonic pumping of pervasive granitic
1104 melts. *Tectonophysics*, *332*(4), 387-402. https://doi.org/10.1016/S0040-1951(00)00297-3

1105 Sylvester, P. J. (1998). Post-collisional strongly peraluminous granites. *Lithos*, *45*(1-4), 29-44.
1106 https://doi.org/10.1016/S0024-4937(98)00024-3

1107 Szymanowski, D., Wotzlaw, J. F., Ellis, B. S., Bachmann, O., Guillong, M., & Von Quadt, A.
1108 (2017). Protracted near-solidus storage and pre-eruptive rejuvenation of large magma
1109 reservoirs. *Nature Geoscience*. https://doi.org/10.1038/ngeo3020

1110 Thomson, K. (2007). Determining magma flow in sills, dykes and laccoliths and their
1111 implications for sill emplacement mechanisms. *Bulletin of Volcanology*, *70*(2), 183-201.
1112 https://doi.org/10.1007/s00445-007-0131-8

1113 Townsend, M.R., Pollard, D.D., Smith, R.P. (2017) Mechanical models for dikes: a third school

of thought. Tectonophysics 703, 98-118

Thordarson, T., & Self, S. (2003). Atmospheric and environmental effects of the 1783–1784 Laki eruption: A review and reassessment. *Journal of Geophysical Research: Atmospheres*, *108*(D1), AAC-7. https://doi.org/10.1029/2001JD002042

Walker, G. P. L. (1989). Gravitational (Density) controls on volcanism, magma chambers and intrusions. *Australian Journal of Earth Sciences*. https://doi.org/10.1080/08120098908729479

Watson, E.B. and Harrison, T.M. (1983) Zircon saturation revisited: temperature and compositional effects in a variety of crustal magma types. Earth and Planetary Science Letters, 64, 295-304.

Wotzlaw, J. F., Bindeman, I. N., Stern, R. A., D'Abzac, F. X., & Schaltegger, U. (2015). Rapid heterogeneous assembly of multiple magma reservoirs prior to Yellowstone supereruptions. *Scientific reports*, *5*, 14026. https://doi.org/10.1038/srep14026

Wotzlaw, J. F., Bindeman, I. N., Watts, K. E., Schmitt, A. K., Caricchi, L., & Schaltegger, U. (2014). Linking rapid magma reservoir assembly and eruption trigger mechanisms at evolved Yellowstone-type supervolcanoes. *Geology*, *42*(9), 807-810. https://doi.org/10.1130/G35979.1

Wotzlaw, J. F., Schaltegger, U., Frick, D. A., Dungan, M. A., Gerdes, A., & Günther, D. (2013). Tracking the evolution of large-volume silicic magma reservoirs from assembly to supereruption. *Geology*, *41*(8), 867-870. https://doi.org/10.1130/G34366.1